Comprehensive Investigation of Quasibrittle Fracture of IM7/977-3 Laminates via Size Effect Analysis

Jiacheng Chen

A dissertation
submitted in partial fulfillment of the
requirements for the degree of

Master of Science in Aeronautics & Astronautics

University of Washington

2023

Reading Committee:
Marco Salviato, Chair
Ramulu Mamidala
Eleftheria Roumeli

Program Authorized to Offer Degree:
Aeronautics & Astronautics

University of Washington

Abstract

Comprehensive Investigation of Quasibrittle Fracture of IM7/977-3 Laminates via Size Effect Analysis

Jiacheng Chen

Chair of the Supervisory Committee:
Marco Salviato
Aeronautics & Astronautics

This thesis investigates the non-linear size effect of fracture of IM7/977-3 laminates with different sizes in multiple modes including the matrix-dominated Mode I intralaminar fracture, the fiber-dominated Mode I intralaminar fracture, the Mode I interlaminar fracture, and the Mode II interlaminar fracture.

The IM7/977-3 laminates, which are composed of HexTow® IM7 carbon fibers and CYCOM® 977-3 epoxy resin, are fabricated in-house using vacuum-bagged autoclave curing. Four types of tests, including Single-Edge Notched Tension (SENT), Double-Edge Notched Tension (DENT), Double Cantilever Beam (DCB), and End-Notched Flexure (ENF), are conducted to examine the fracture in the above-mentioned modes. In addition, Digital Image Correlation (DIC) is used to visualize the stain localization near the crack tip of DCB and ENF coupons.

The load-displacement curve of each is recorded to obtain its fracture load. Based on the test results, with the assistance of the finite element method and Bažant's size effect law, key parameters, including the fracture energy, the effective Fracture Processing Zone (FPZ) size, the pseudo-plastic limit, and the characteristic size are determined.

Significant non-linearity is observed for the matrix-dominated Mode I intralaminar fracture, the fiber-dominated Mode I intralaminar fracture, and the Mode II interlaminar frac-

ture. Therefore, compared to the conventional Linear Elastic Fracture Mechanics (LEFM), this study provides a more accurate prediction of fracture load of IM7/977-3 laminates in these modes at any size. The outcome of this study can be utilized to further optimize the structures made of IM7/977-3 laminates to get better performance.

TABLE OF CONTENTS

LIST OF FIGURES

GLOSSARY

CFRP: Carbon Fiber Reinforced Polymer

CLT: Classical Laminate Theory

CTE: Coefficient of Thermal Expansion

DCB: Double Cantilever Beam

DENT: Double Edge Notched Tension

DIC: Digital Image Correlation

ECT: Edge Crack Torsion

ENF: End Notched Flexure

FEA: Finite Element Analysis

FEM: Finite Element Method

FPZ: Fracture Process Zone

IM7: HexTow® IM7 Carbon Fiber

LEFM: Linear Elastic Fracture Mechanics

ROM: Rule of Mixture

SENT: Single Edge Notched Tension

SEL: Bažant Size Effect Law

UW: University of Washington

977-3: CYCOM® 977-3 Epoxy Resin

ACKNOWLEDGMENTS

I would like to acknowledge my faculty advisor Prof. Salviato, and my committee members Prof. Mamidala and Prof. Roumeli for their guidance and support during the project. Without their effort, I would not have had the opportunity to get involved in such an interesting and ambitious project.

A special thanks to my colleague Sean Phenisee for his great mentorship. Without his encouragement and knowledge, I can hardly make such a complete and systematic study. I would also like to thank my colleague Antonio Deleo, Jiahao Lu, Genki Matsubara, Troy Nakagawa, and Yusuf Rasyid. It is impossible to finalize this study within a single quarter without their great assistance.

I would like to thank the University of Washington staff Kameron Harmon and Bill Kuykendall. The training and assistance they provided are essential to the successful completion of specimen fabrication and testing.

Thanks to all my loved ones for supporting me all the way through my toughest times. Your support is my greatest backing to overcome any difficulty.

Lastly, I dedicate my most sincere thanks to my grandfather. Thank you for all the love and nurturing you had given me over the past 25 years. May your departed soul find solace in heaven.

Chapter 1
INTRODUCTION

1.1 Introduction of CFRP: Strengths, Weaknesses, and Applications

Carbon Fiber Reinforced Polymer, abbreviated CFRP, is a type of composite that consists of polymer and carbon fibers. Carbon fibers serve as the reinforcement and undertake most of the load, while polymer serves as the matrix which binds the carbon fibers and transfers the load among fibers. To provide the maximum stiffness and strength in the designated direction, the carbon fibers in CFRP are usually aligned. Due to the difference in mechanical properties between carbon fibers and polymers, CFRPs have their unique anisotropic mechanical behavior.

As shown in Fig. 1.1, the greatest advantage of CFRP is its high specific modulus and strength, which greatly outperforms regular aerospace materials such as aluminum alloys. Due to these advantages, currently, the demand for CFRP in the fields such as aerospace, automobile, and energy is growing tremendously. For instance, as shown in Fig. 1.2, over 50% of the weight of modern aircraft such as Airbus A350 XWB is made of composite, which is mainly CFRP. The weight-saving feature of CFRP enables larger load capacity, fuel economy, and better flight riding experience.

However, the CFRP has its own drawbacks. One of the most significant drawbacks is the non-linear size effect on the fracture load of CFRP, making the prediction of fracture load more complicated.

1.2 Completed Research

Since IM7/977-3 is one of the most used CFRPs in the industry, multiple studies are done to investigate its basic mechanical properties. Clay et al. used multiple ASTM standardized

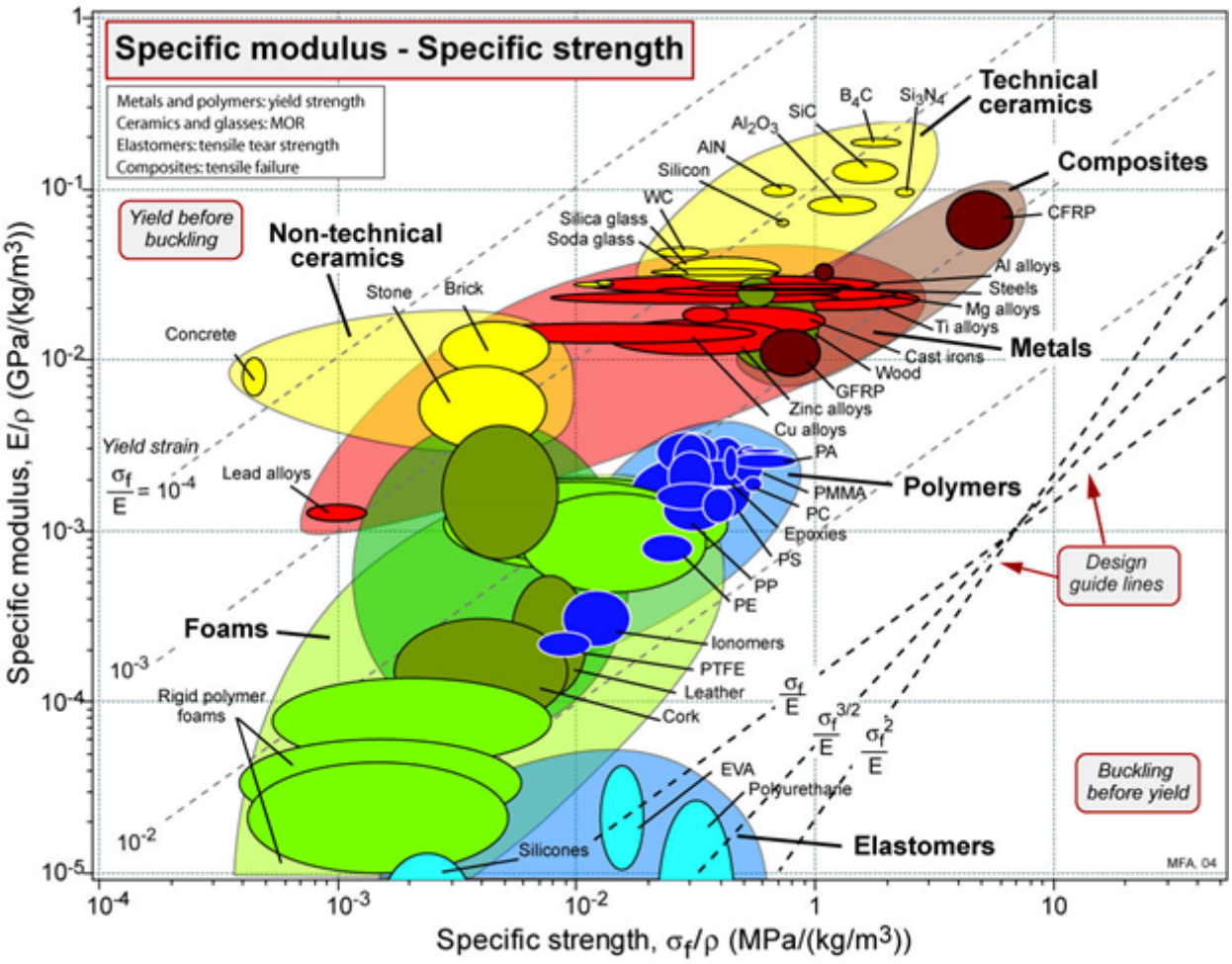

Figure 1.1: The plot of specific modulus versus specific strength of common materials [3]

tests and characterization methods to examine the mechanical performances of unnotched and notched laminates with different layup designs. Clay et al. also tried to estimate the fracture energy of the IM7/977-3 material based on the method provided in the ASTM handbook, but due to the non-linear size effect of the fracture load of CFRPs, the equations given in the ASTM handbook significantly overpredict the fracture load. [11]

Meanwhile, pioneered by Z. P. Bažant, the investigation of the non-linear size effect of CFRPs has become a popular research topic since the 1980s. A study conducted by Salviato

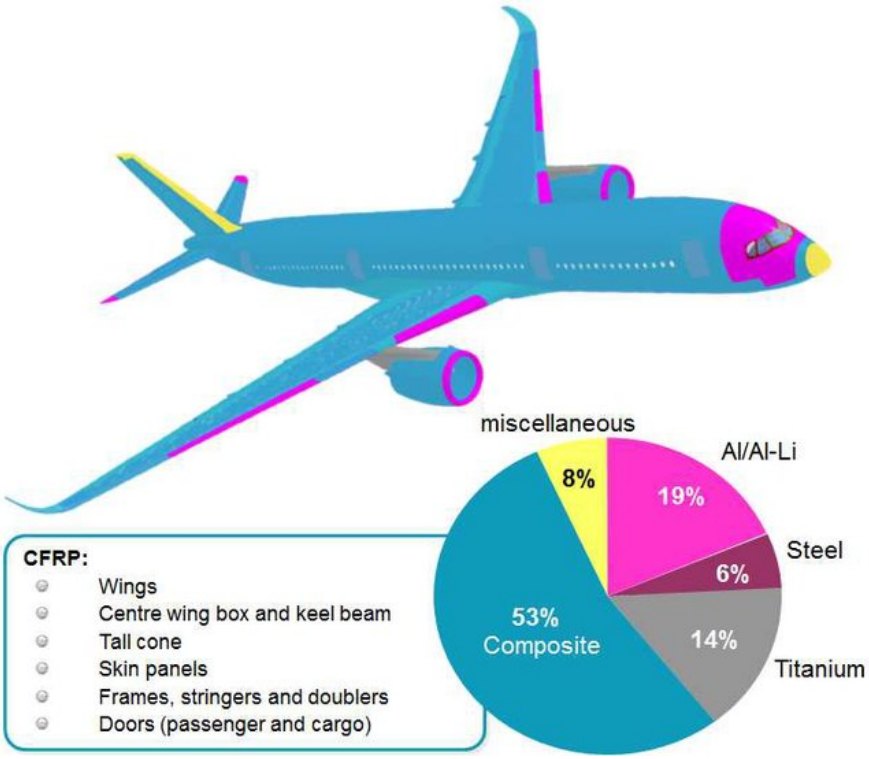

Figure 1.2: The usage of materials on Airbus A350 XWB [7]

et al. investigated the size effect on the interlaminar fracture of $[0]_8$ and $[45]_8$ carbon fiber-reinforced DGEBA-based epoxy resin laminates. The study reveals the non-linear size effect of the fracture of the above-mentioned CFRP. [36, 32, 31, 9, 22]. Similar conclusions can be drawn based on work on 2D textile composites [35, 34], 3D textile composites [24], chopped fiber composites [18, 20, 17, 26, 19], polymers [14, 29, 28], polymer nanocomposites [25, 30], and even wood [27].

1.3 Motivation and Objectives

The non-linear size effect of composites can greatly affect the design of composite-made products, such as aircraft. As shown in Fig. 1.3, the structural design of an aircraft is based on coupon tests. The engineers estimate the mechanical behavior of the aircraft based on the scaling of coupons. However, due to the non-linear size effect of CFRPs, the scaling

based on Linear Elastic Fracture Mechanics (LEFM) leads to inaccurate estimation of the fracture behavior of the aircraft parts. In this case, a conservative design with a large factor of safety must be used to make sure the structure is able to withstand the designated load. The conservative design greatly offsets the weight-saving advantages of CFRPs.

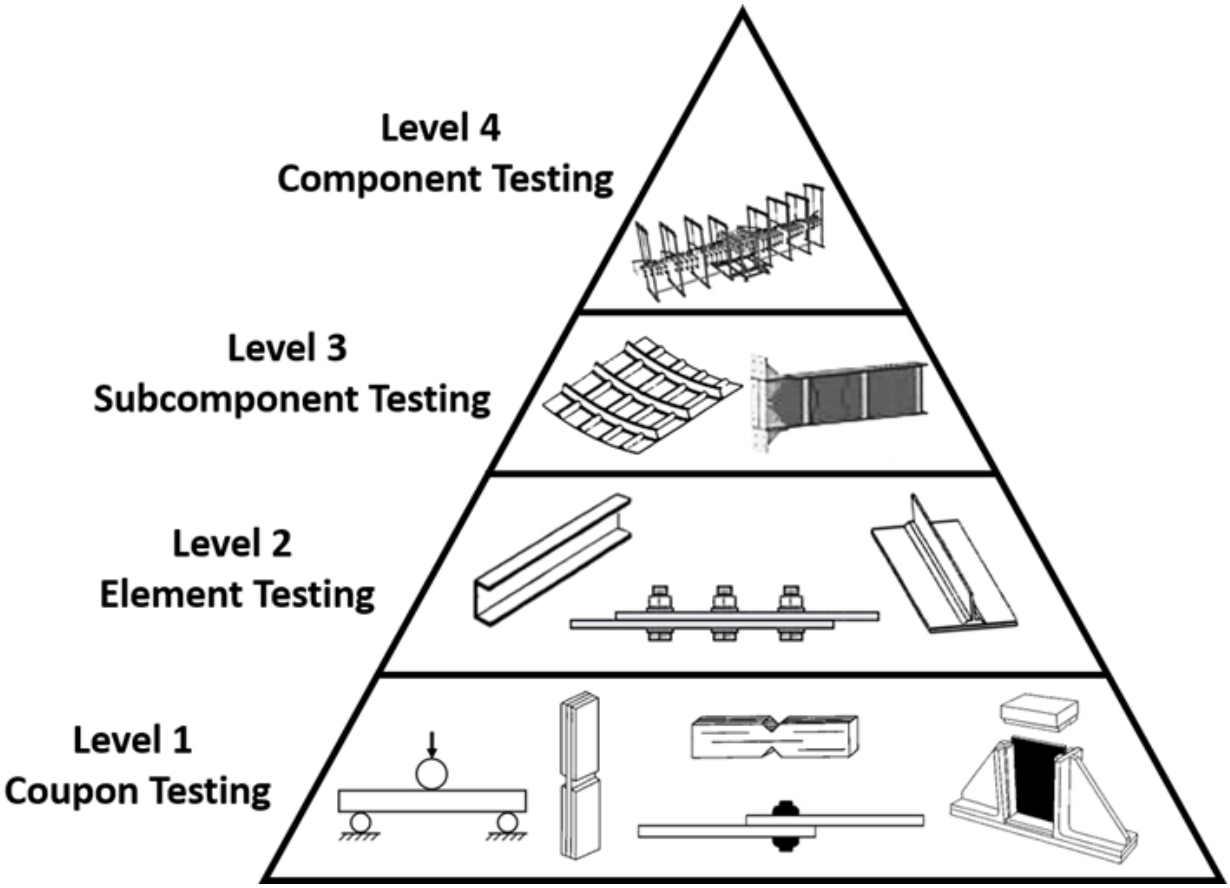

Figure 1.3: The building block approach of composite-made aircraft [1]

The Air Force Research Lab (AFRL) would like to use IM7/977-3 on aircraft, and accurate prediction of the non-linear size effect of the fracture behavior of IM7/977-3 is necessary to optimize the design of the structure and improve the performance.

Therefore, this thesis aims to analyze the non-linear size effect of fracture of IM7/977-3 laminates in different modes by multiple mechanical tests. Based on the test results, a non-

linear size effect curve can be constructed to accurately predict the fracture of IM7/977-3 at any size. The outcomes of this thesis can be utilized on any IM7/977-3-made aircraft for structural optimization and performance improvement.

Chapter 2

FUNDAMENTAL THEORIES

This chapter aims to introduce the key theories that are used in the size-effect analysis of fracture mechanics of IM7/977-3 laminates.

2.1 CLT

CFRP laminates are generally anisotropic, meaning that the material properties are direction-dependent, so Classical Laminate Theory, abbreviated as CLT, is established to model the deformation of laminate at in-plane loading conditions assuming linear elastic behavior. [21] CLT models a single ply as a transversely isotropic material that can be characterized by 4 quantities including E_1, E_2, ν_{12} and G_{12}. "1" refers to the direction of aligned fibers while "2" is the in-plane direction perpendicular to "1". The in-plane stress state and strain state of a single ply can be related by the global stiffness $\left[\bar{Q}\right]$:

$$\left[\bar{Q}\right] = \frac{1}{1-\frac{E_2}{E_1}\nu_{12}^2}\begin{bmatrix} c^2 & s^2 & -2cs \\ s^2 & c^2 & 2cs \\ cs & -cs & c^2-s^2 \end{bmatrix}\begin{bmatrix} E_1 & \nu_{12}E_2 & 0 \\ \nu_{12}E_2 & E_2 & 0 \\ 0 & 0 & G_{12} \end{bmatrix}\begin{bmatrix} c^2 & s^2 & cs \\ s^2 & c^2 & -cs \\ -2cs & 2cs & c^2-s^2 \end{bmatrix} \tag{2.1}$$

where c and s refers to $\sin\theta$ and $\cos\theta$ respectively, and θ refers to the angle between the local direction "1" and the global direction "x". Based on the stiffness matrix, CLT relates

the in-plane strain, curvature, and in-plane loads of a laminate plate by:

$$\begin{Bmatrix} N_x \\ N_y \\ N_{xy} \end{Bmatrix} = [A] \begin{Bmatrix} \epsilon_x^o \\ \epsilon_y^o \\ \gamma_{xy}^o \end{Bmatrix} + [B] \begin{Bmatrix} \kappa_x \\ \kappa_y \\ \kappa_{xy} \end{Bmatrix}$$
$$\begin{Bmatrix} M_x \\ M_y \\ M_{xy} \end{Bmatrix} = [B] \begin{Bmatrix} \epsilon_x^o \\ \epsilon_y^o \\ \gamma_{xy}^o \end{Bmatrix} + [D] \begin{Bmatrix} \kappa_x \\ \kappa_y \\ \kappa_{xy} \end{Bmatrix} \tag{2.2}$$
$$[A] = \sum_{i=1}^{n} [\bar{Q}]_i (z_i - z_{i-1})$$
$$[B] = \frac{1}{2} \sum_{i=1}^{n} [\bar{Q}]_i (z_i^2 - z_{i-1}^2)$$
$$[D] = \frac{1}{3} \sum_{i=1}^{n} [\bar{Q}]_i (z_i^3 - z_{i-1}^3)$$

where $\{N_x \ N_y \ N_{xy}\}^T$ are the planar normal and shear load per unit length, $\{M_x \ M_y \ M_{xy}\}^T$ are the planar bending and torsion load per unit length, $\{\epsilon_x^o \ \epsilon_y^o \ \gamma_{xy}^o\}^T$ are the mid-plane strains, $\{\kappa_x \ \kappa_y \ \kappa_{xy}\}^T$ are the curvatures, i corresponds to the ply counted from bottom to top, and z is the distance between the mid-plane of the ply to the mid-plane of the laminate. In this study, CLT is used to model the equivalent homogeneous material properties of a non-unidirectional laminate.

2.2 Modes of Fracture

The propagation of a crack can be described as a combination of three basic modes, as shown in Fig. 2.1. The first mode is called the opening mode, caused by tensile stress normal to the crack plane. The second mode is called the sliding mode, caused by shear stress parallel to the crack plane and in the direction of crack propagation. The third mode is called the tearing mode, caused by shear stress perpendicular to both the crack plane and the direction of propagation. These three modes have different effects on the stress distribution around the crack, and a material's resistance to the three types of crack propagation can be very

different from each other. In this study, the mode I intralaminar fracture, and mode I and II interlaminar fracture are investigated.

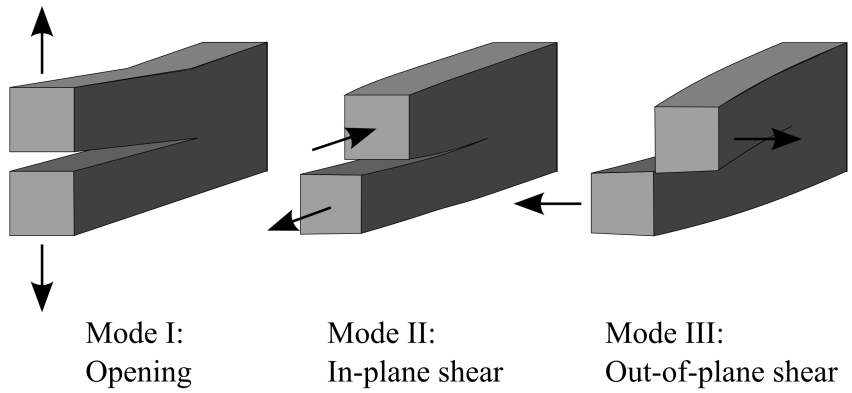

Figure 2.1: The three modes of fracture [2]

2.3 Energy Release Rate and J-integral

The crack propagation can be modeled as a conservation of energy. In order to propagate a crack, the energy available, which is the difference between the work done on the material and the strain energy stored in the material, must equal the energy required to create the new crack surface. In fracture mechanics, G is defined as the energy release rate, which is equal to the energy available per unit crack area. Based on the definition of G

$$Gb\delta a = \delta W - \delta U \tag{2.3}$$

where b is the thickness of the material, a is the crack length, W is the work done on the material, and U is the strain energy stored in the material. [16] The crack starts to propagate if G approaches the fracture energy, G_c, which is a material property, and its determination is a major objective of this study.

There are multiple ways to compute G, and the one used in this study is called J-integral

[33], which is defined as

$$J = \int_{\Gamma} \left(\bar{u} dx_2 - \vec{t} \cdot \frac{\partial \vec{u}}{dx_1} ds \right) \tag{2.4}$$

where Γ is an arbitrary counterclockwise path around the crack, $\bar{u}$ is the strain energy density, $\vec{t}$ is the 2D traction vector, and $\vec{u}$ is the 2D displacement vector. It can be mathematically proved that $J \equiv G$. The J-integral is a convenient method to evaluate the G if the stress and strain states around the crack can be determined, which can be realized by the finite element method.

2.4 LEFM

Linear Elastic Fracture Mechanics, abbreviated as LEFM, is the first fracture mechanics developed to describe the fracture of brittle material. Assuming the material is purely linear elastic, Wastergaard developed a solution to describe the stress near the crack tip. For example, the y-direction stress σ_{yy} around the crack tip under a mode I loading with distant stress σ_{∞} can be expressed as:

$$\sigma_{yy} = \frac{\sigma_{\infty}\sqrt{\pi a}}{\sqrt{2\pi r}} \cos\frac{\theta}{2} \left[1 + \sin\frac{\theta}{2} \sin\frac{3\theta}{2} \right] \tag{2.5}$$

where r and θ are the polar coordinates originating at the crack tip. This equation shows that at the crack tip, stress approaches infinity. [38] Therefore, instead of the stress at the crack tip, a parameter called the stress intensity factor, abbreviated SIF, is introduced to characterize the stress field near the tip. SIF of mode I can be expressed as:

$$K_I = \lim_{r \to 0} \sigma_{yy} \sqrt{2\pi r} = Y \sigma_{\infty} \sqrt{\pi a} \tag{2.6}$$

where Y is the geometric correction factor.

In LEFM, the material fractures when K exceeds the fracture toughness of the material, with the symbol K_c. SIF is also related to the energy release rate by:

$$G_I = \frac{K_I}{E'} \tag{2.7}$$

$$G_{II} = \frac{K_{II}}{E'} \tag{2.8}$$

where E' is the effective Young's modulus and G is the shear modulus. The relationship also applies to K_c and G_c.

The greatest limitation of LEFM is the stress singularity at the crack tip, which only applies to the stress state of brittle material. The ductile materials yield near the crack tip and form the plastic zone, abbreviated as PZ, so the stress stays at the yield strength σ_y in PZ. For quasibrittle materials, the stress descends while approaching the crack tip due to the fracture process zone, abbreviated as FPZ. The demonstration of PZ and FPZ, as well as the stress curves near the crack tips of three types of materials are displayed in Fig. 2.2.

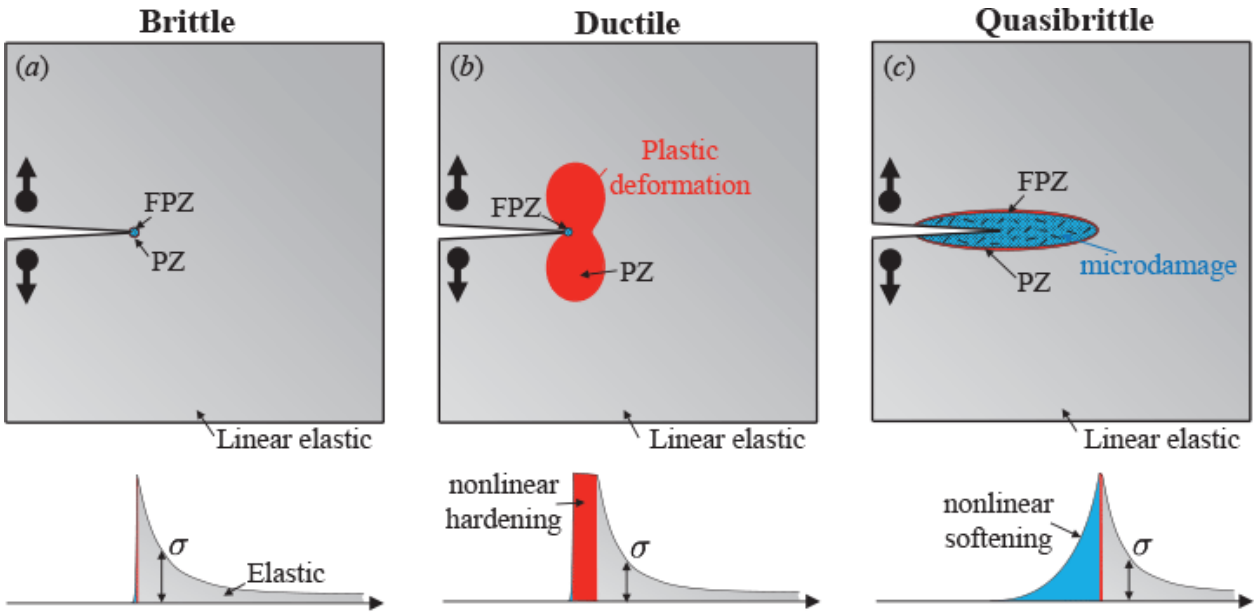

Figure 2.2: The fracture behavior of (a) brittle, (b) ductile, and (c) quasibrittle material. [8]

2.5 Quasibrittle Materials and FPZ

Quasibrittle materials are heterogeneous materials with brittle constituents. Typical quasibrittle materials include composites such as concrete, wood, and fiber-reinforced polymer. Different from typical brittle (e.g. ceramics) and ductile (e.g. aluminum alloy) materials, when a notched quasibrittle material is loaded, microcracks, frictional micro-slips, and grain

interlock form near the crack tip and soften and material around the crack tip. This long and wide region is called the fracture process zone, abbreviated as FPZ. Different from PZ of ductile material, which size depends on the loading condition, the size of FPZ is a material property. When the size of FPZ is comparable to the size of the quasibrittle material, the fracture behavior will highly deviate from the prediction of LEFM. Therefore, it is important to study the FPZ size of quasibrittle materials to predict their fracture behaviors.

2.6 Size Effect

As introduced in the previous section, the FPZ can greatly affect the fracture of quasibrittle material. To characterize the effect of FPZ on quasibrittle material of different sizes, a size effect analysis is necessary. In the size effect analysis, a new parameter called nominal strength, with symbol σ_{Nc}, is introduced. This parameter relates the load at fracture and the geometry of the structure and is not necessarily representing any physical stress on the structure. According to dimension analysis, σ_{Nc} is inversely proportional to $\sqrt{1 + D/D_0}$, where D represents the size of the structure while D_0 is the reference size. Bažant et al. derived that

$$\sigma_{Nc} = B f_t' \left(1 + \frac{D}{D_0}\right)^{-\frac{1}{2}} \tag{2.9}$$

where f_t' is the strength of the material and B is a dimensionless parameter. [10] Fig. 2.3 demonstrates how the Bažant size effect law (SEL) works. Large-sized structures behave similarly to brittle materials, while small-sized structures behave similarly to ductile materials. Based on Irwin's relation and first-order Taylor expansion, Eq. 2.9 can be rewritten as

$$\sigma_{Nc} = \sqrt{\frac{E' G_c}{D g(\alpha_0) + C_f g'(\alpha_0)}} \tag{2.10}$$

where $\alpha_0 = a_0/D$. The parameter C_f is the effective FPZ length, which represents the size of FPZ. The parameter g is called the dimensionless energy release rate, which is determined by

$$g = \frac{G E'}{\sigma_{Nc}^2 D} \tag{2.11}$$

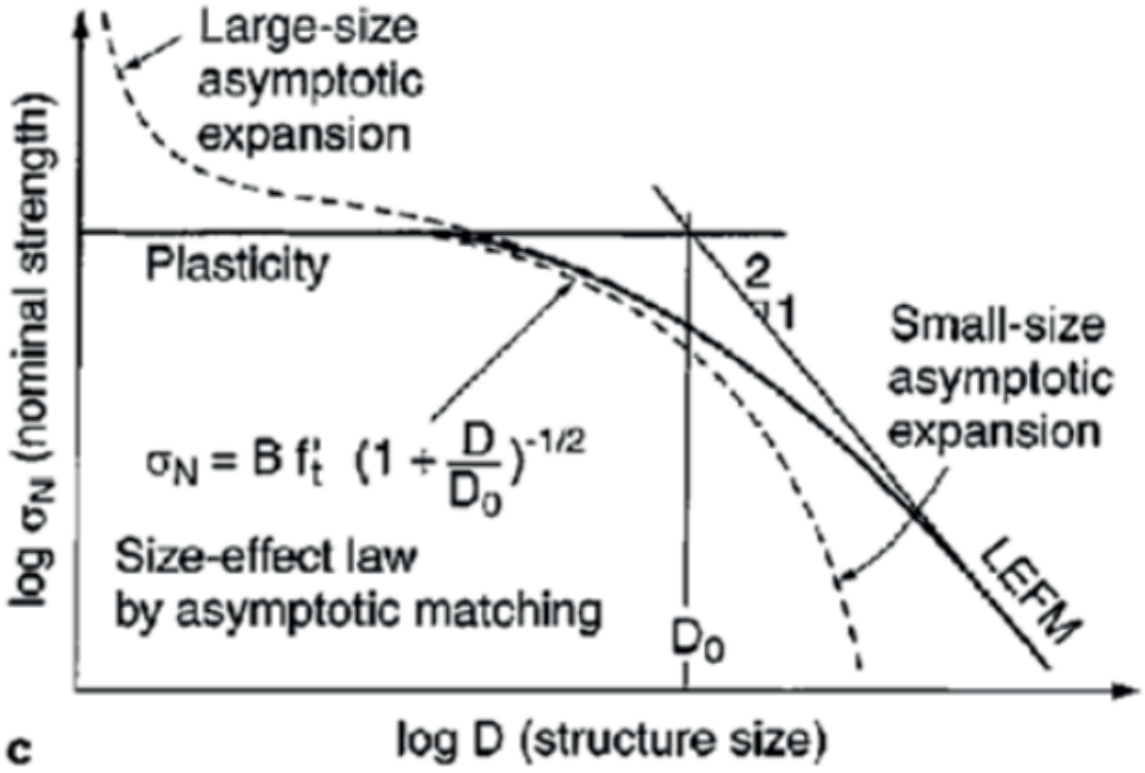

Figure 2.3: The Bažant size effect law of quasibrittle fractures

And the derivative g' can be estimated by the finite difference method:

$$g'(\alpha_o) = \frac{g(\alpha_0 + \Delta\alpha) - g(\alpha_0 - \Delta\alpha)}{2\Delta\alpha} \tag{2.12}$$

where $\Delta\alpha/\alpha_0 \sim 0.005$.

One key feature of this parameter is that for structures made of the same material, if their geometries are similar to each other (same *alpha* and same aspect ratio D/L), both g and its derivative g' stay constant. If g and g' of a specific shape can be obtained, G_c and C_f can be determined via linear fitting of test data:

$$Y = \frac{1}{\sigma_{Nc}^2} = \frac{g(\alpha_0)}{E'G_c}D + \frac{C_f g'(\alpha_o)}{E'G_c} = A \times D + B \tag{2.13}$$

$$G_c = \frac{g(\alpha_0)}{E'A} \tag{2.14}$$

$$C_f = \frac{g(\alpha_0)}{g'(\alpha_o)} \cdot \frac{B}{A} \tag{2.15}$$

The pseudo-plastic limit is the horizontal asymptote of the size effect law curve. It is the upper limit of nominal stress of extremely small-sized structures and can be determined by:

$$\sigma_0 = \sqrt{\frac{E'G_c}{C_f g'(\alpha_o)}} \tag{2.16}$$

And the characteristic size is the intersection between the pseudo-plastic limit and the LEFM curve. It is determined by:

$$D_0 = C_f \frac{g'(\alpha_o)}{g(\alpha_0)} \tag{2.17}$$

Based on the characteristic size, the brittleness of the material, which defines whether a material behaves more brittle or ductile, is determined by:

$$\beta = \frac{D}{D_0} \tag{2.18}$$

Once G_c and C_f are determined, the size effect law can make a good prediction of the fracture behavior at any size.

Chapter 3
MATERIAL AND MANUFACTURING

This chapter aims to introduce the material properties of IM7/977-3 laminates, the test coupons used for size-effect analysis, and the in-house fabrication of the laminates.

3.1 Overview of IM7/977-3 Properties

The CFRP studied in this project consists of IM7 fiber and 977-3 thermoset polymer. IM7 fiber is a continuous, high-performance, and intermediate modulus PAN-based fiber. 977-3 is a thermoset epoxy formulated for autoclave and press molding curing. Clay et al. have determined the basic mechanical properties of a typical IM7/977-3 composite that is similar to the material used in this study. Table. 3.1 lists the mechanical properties determined by Clay et al. and are used in this study. Assuming transverse isotropy, it is estimated that $E_{3T} = E_{2T}$ and $\nu_{13} = \nu_{12}$.

Property	Symbol	Mean±SD
Tensile longitudinal modulus (GPa)	E_{1T}	164±4.12
Tensile transverse modulus (GPa)	E_{2T}	8.98±0.284
In-plane shear modulus (GPa)	G_{12}	5.01±0.249
Major Poisson's ratio	ν_{12}	0.320±0.0266

Table 3.1: Basic Mechanical Properties of Unidirectional IM7/977-3 Laminate [11]

3.2 Laminate Fabrication

The overall manufacturing procedures of IM7/977-3 laminates are displayed in Fig. 3.1.

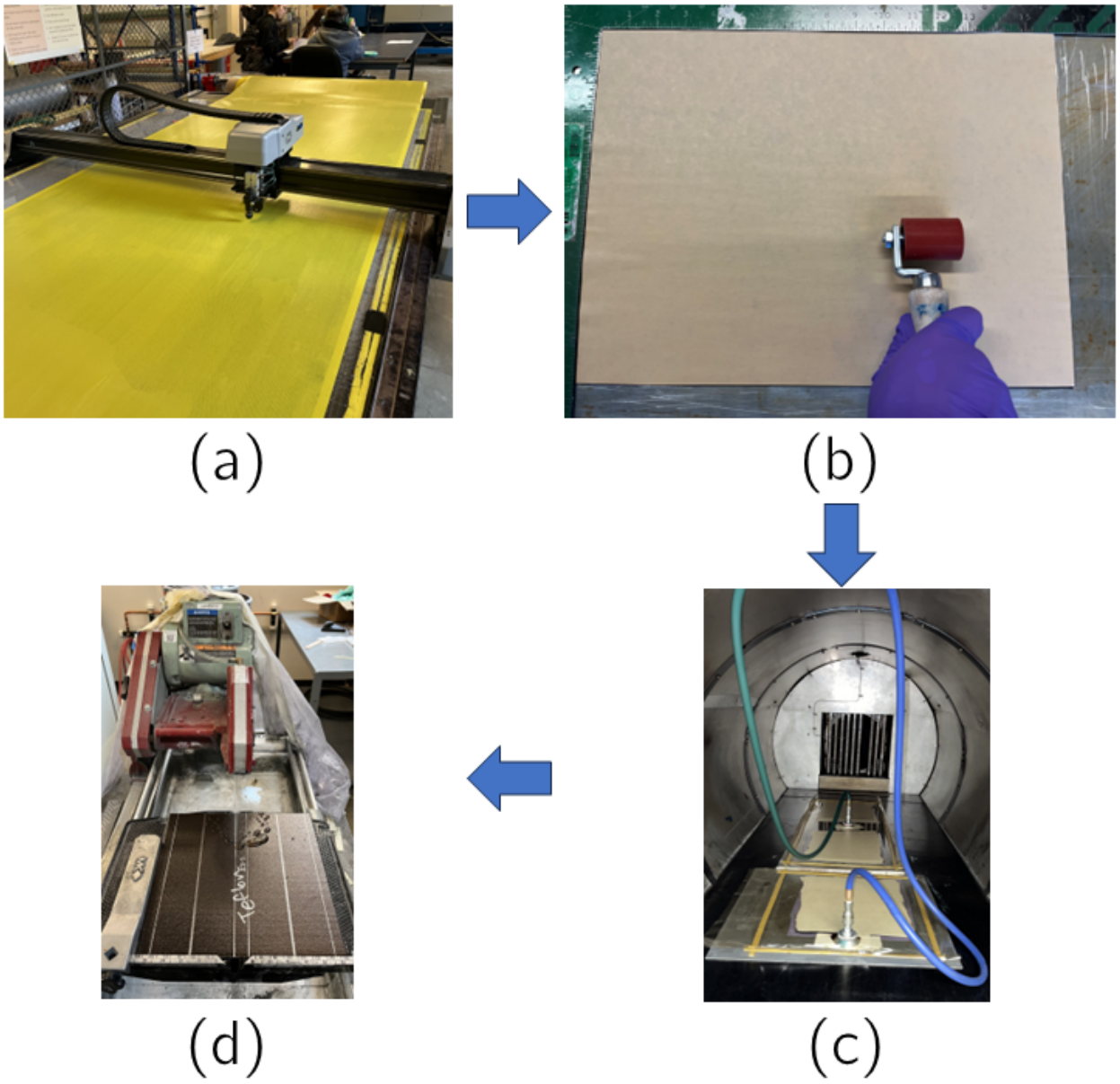

Figure 3.1: The manufacturing procedures of IM7/977-3 laminates. (a) Prepreg cutting; (b) Hand lay-up; (c) Vacuum bagging and autoclave curing; (d) Coupon cutting

The IM7/977-3 laminate plates are fabricated from the corresponding prepregs, which refers to the rolled film of aligned IM7 fibers mixed with uncured 977-3. The prepreg roll is stored in the freezer when unused to reduce the rate of procuring and extend the shelf

life. It is thawed at ambient temperature for approximately 1 hour prior to working. Once the prepreg roll is fully thawed, it is cut into small rectangular plies via an Autometrix Advantage CNC cutter. The cut prepreg plies are then laid up on an aluminum tooling plate and vacuum bagged following the material sandwich method demonstrated in Fig. 3.2. Table. 3.2 lists the bagging material used in IM7/977-3 laminate fabrication. It is important to know that the vacuum bagging materials can slightly affect the laminate properties.

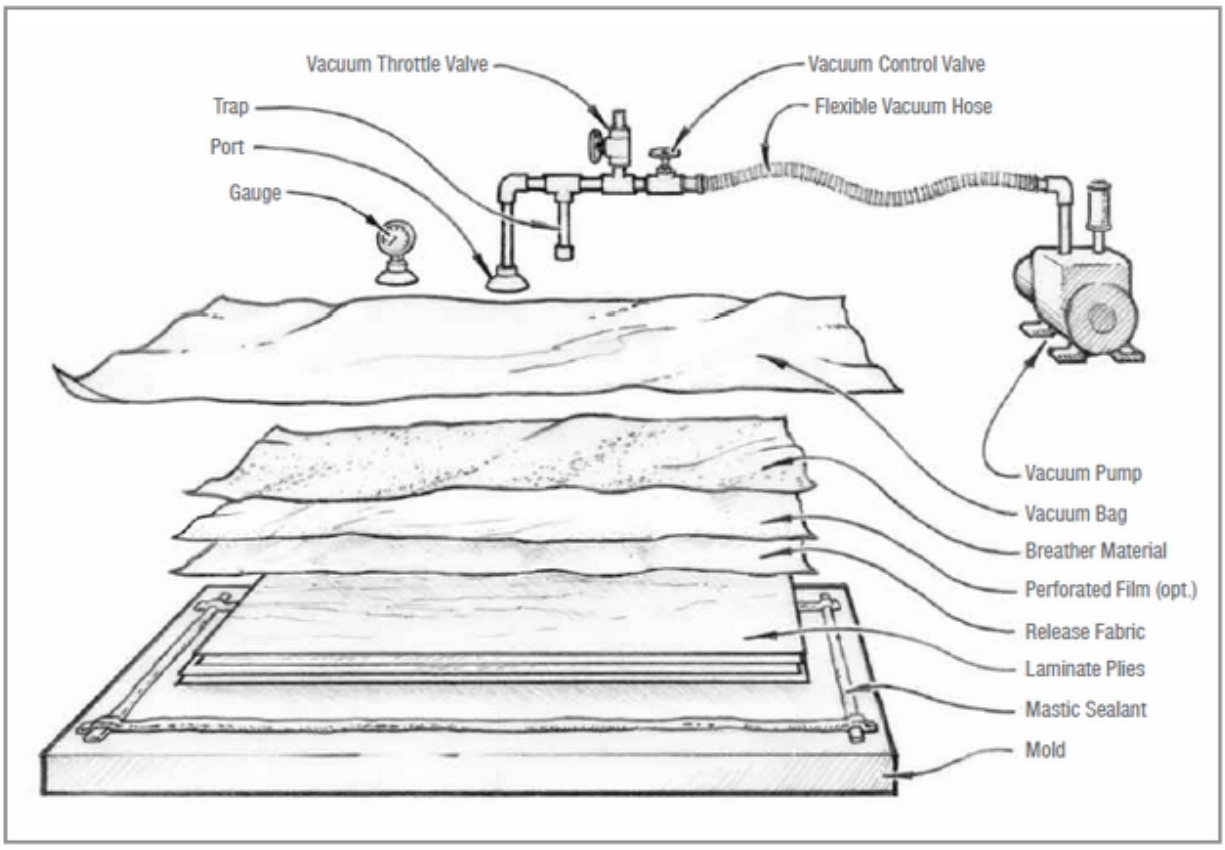

Figure 3.2: Schematics of a sandwich layup for vacuum bagging [13]

For the laminates used for DCB and ENF testing, at the halfway of laying up, the laid up prepregs are vacuum debulked for 1 hour. Then the Teflon film is placed on the prepreg before continuing to lay up. Fig. 3.3 is a photo of a DCB coupon after testing, showing how the Teflon film is placed in the middle of the laminate. After finishing laying up, another

Type	Manufacturer	Product
Vacuum Bagging Film	Airtech	Wrightlon® WL7400
Release Film	Airtech	A4000
Breather Cloth	Airtech	Airweave® N10
Release Agent	Airtech	Release All® Safelease 30
Interlaminar Film	American Durafilm	0.0005" Teflon® FEP Film

Table 3.2: Materials Used in Vacuum Bagging Sandwich Structure

1-hour vacuum debulking is performed. The vacuum debulking process minimizes the voids that exist in the laminate, which may significantly affect the interlaminar fracture testing.

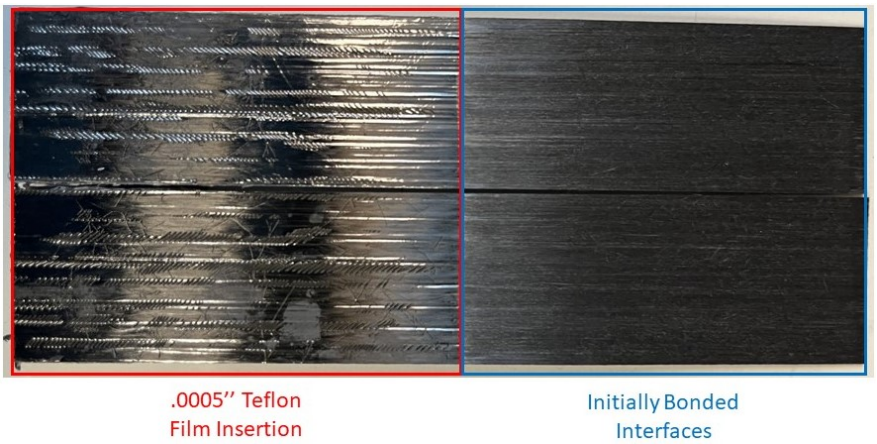

Figure 3.3: Seperated half-DCB coupons after the test. The shiny regions are the location of Teflon insertion.

The laid up prepregs are then cured in American Autoclave Co. autoclave under the manufacturer's recommended recipe, shown in Fig. 3.4. The actual curing is slightly different from the preset temperature curve, as in the cooling stage, the temperature descends in an exponential way following the heat transfer law. The laminates are then taken out from the autoclave and removed from the tooling plate. From Fig. 3.3, it is observed that the Teflon

film is not perfectly flat because of fiber extruding out from the prepreg and CTE difference between Teflon and prepreg. This may slightly affect the DCB and ENF test results.

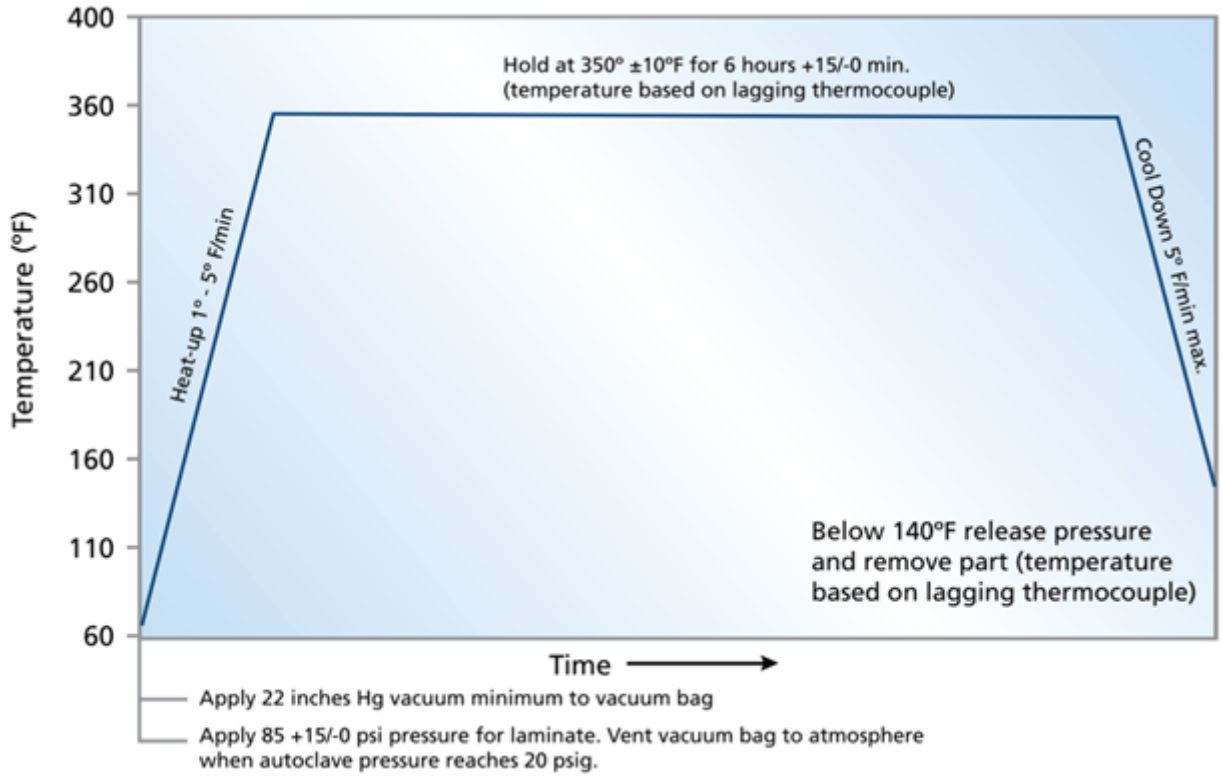

Figure 3.4: The manufacturer's recommended curing recipe of 977-3 epoxy [12]

The last stage is to cut the laminates into test coupons. An MK Diamond Products MK 101 wet tile saw is used to cut the fibers. It is observed that the fibers at the cutting edge on the rear surface are stretched out (as shown in Fig. 3.5), which may slightly affect the SENT test results.

3.3 Coupon Design and Fabrication

Four types of tests are conducted to examine the fracture mechanics of IM7/977-3 in both intralaminar and interlaminar directions, including Single-Edge Notched Tension (SENT) test of $[90]_{12}$ laminate coupons, Double-Edge Notched Tension (DENT) test of $[0/90_5]_s$

Figure 3.5: Zoomed photo of a SENT coupon. The fibers in the red box are stretched while being cut.

laminate coupons, Double Cantilever Beam (DCB) and End Notch Flexure (ENF) tests of 0-degree unidirectional laminate coupons.

3.3.1 SENT Tests of IM7/977-3 $[90]_{12}$ *Laminates*

SENT tests of IM7/977-3 $[90]_{12}$ laminates are conducted to examine the matrix-dominated Mode I intralaminar fracture of IM7/977-3 laminates. The schematics of the test coupons, including the dimensions are shown in Fig. 3.6. Table. 3.3 lists the dimensions of the three sizes of SENT coupons being tested.

Due to the design of the load frame tension fixtures, as shown in Fig. 3.7, the maximum thickness of the test coupons is restricted and the tabs cannot be attached to the gripping zone. In order to avoid compression due to the contact between the coupon and the end of the gripping fixture, the length of the gripping zone is designed to be 20 mm, which is close to the maximum gripping length of the fixture. Furthermore, for the large-sized coupons, in order to avoid contact between the coupon and the bolts on both sides of the fixture, the

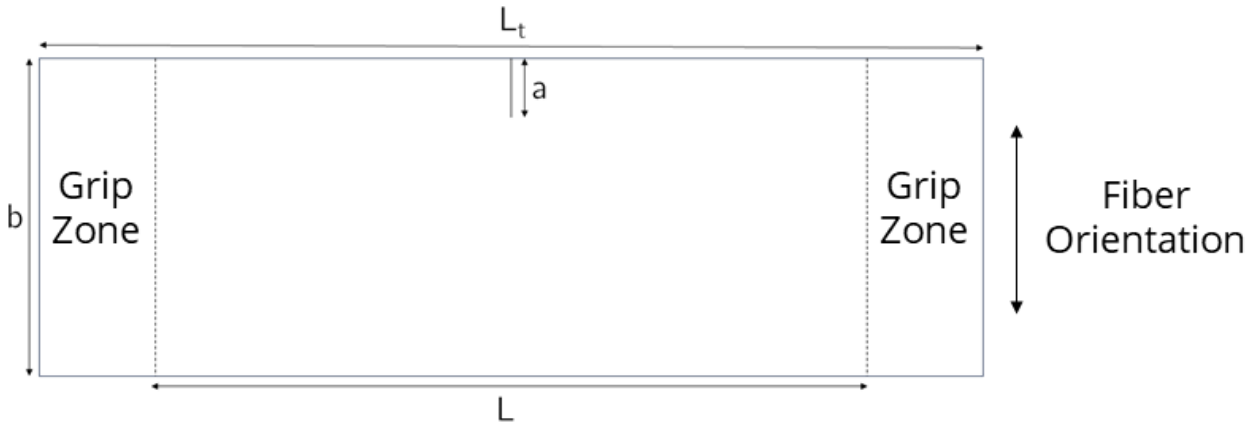

Figure 3.6: Schematics of SENT coupons

Size	L (mm)	L_t (mm)	b (mm)	$AR = L/b$	a_0	$\alpha_0 = a_0/b$	h (mm)
S	25	65	12.5	2	2.5	0.2	1.68
M	50	90	25	2	5	0.2	1.68
L	100	140	50	2	10	0.2	1.68

Table 3.3: Designated Dimensions of SENT Coupons

corners of the coupons are cut, as shown in Fig. 3.8.

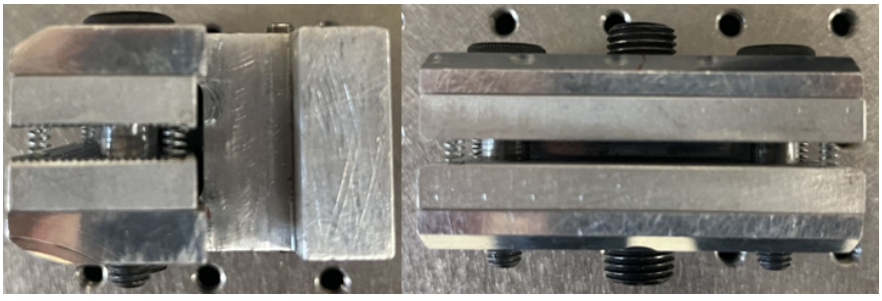

Figure 3.7: The tension fixture used in SENT tests

The notch is cut by ZONA® Fine Kerf Razor Saw, which has a thickness of 0.02" and fineness of 32 teeth per inch. It is discovered that due to the low fracture toughness of the

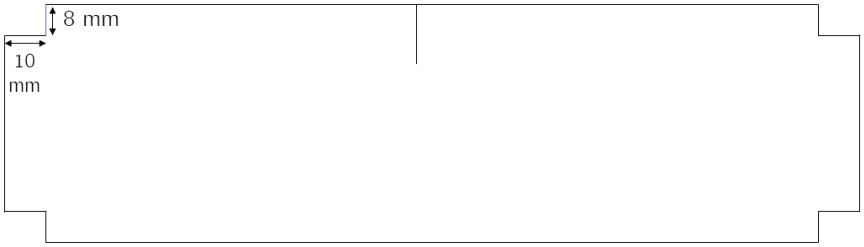

Figure 3.8: Schematics of large-sized SENT coupons

Figure 3.9: The extra damage created while cutting the notch. The blue circle is the notch cut by the razor saw, and the red circle is the extra barely visible damage in front of the crack tip.

977-3 matrix, while cutting the notch, barely visible damage can form at the crack tip, as shown in Fig. 3.9. The extra damage is formed due to the flexure deformation caused by the back-and-forth motion of the saw, and the crack opening caused by the downward force exerted by the saw. The existence of the extra damage lowers the load at fracture, and increases the scatter of the experiment data, making the size-effect analysis less reliable. To minimize the damage, the coupon is slowly cut with minimized downward force while being fixed on a stand to minimize the flexure and crack opening, as shown in Fig. 3.10.

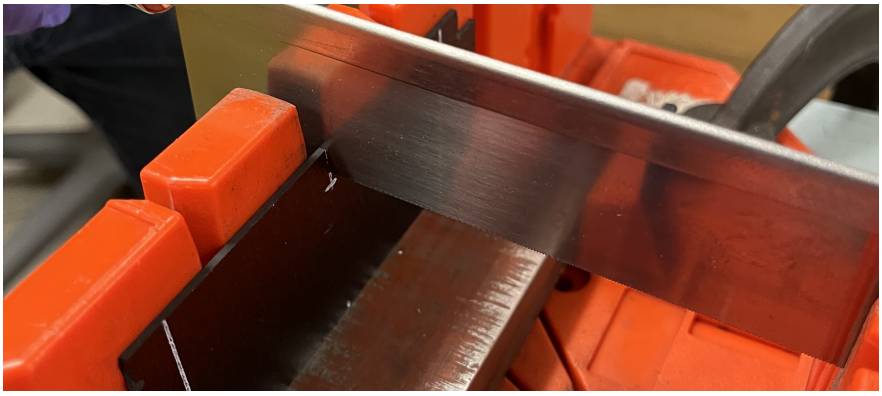

Figure 3.10: Cutting the notch on SENT coupons

3.3.2 DENT Tests of IM7/977-3 $[0/90_5]_s$ Laminates

SENT tests of IM7/977-3 $[0/90_5]_s$ laminates are conducted to examine the fiber-dominated Mode I intralaminar fracture of IM7/977-3 laminates. Because the fracture of fibers is highly randomized, involving multiple extra forms of energy dissipation (e.g. fibers detaching the matrix), and can hardly create a horizontal crack, two notches are required to guide the direction of crack propagation, and ten 90-degree plies are added between two 0-degree plies to minimize the contribution of other energy dissipation forms.

The schematics of the test coupons, including the dimensions are shown in Fig. 3.6. Table. 3.4 lists the dimensions of the three sizes of DENT coupons being tested. Note that a_o is the sum of the lengths of two notches.

Size	L (mm)	L_t (mm)	b (mm)	$AR = L/b$	a_0	$\alpha_0 = a_0/b$	h (mm)
S	50	130	12.5	4	2.5	0.2	1.68
M	100	180	25	4	5	0.2	1.68
L	200	280	50	4	10	0.2	1.68

Table 3.4: Designated Dimensions of DENT Coupons

Because the fiber-dominated Mode I requires a higher load, the gripping pressure needs

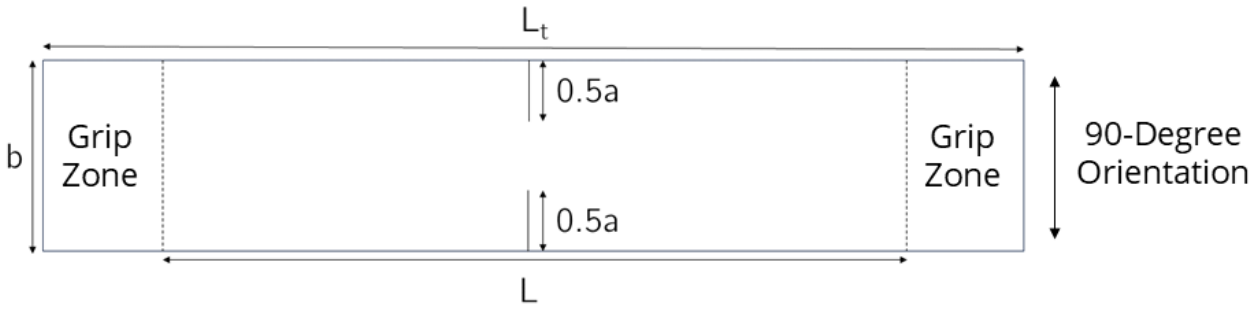

Figure 3.11: Schematics of DENT coupons

to be increased to avoid slipping. In order to prevent laminate crushing under the large gripping pressure, tabs are attached to the gripping zone. The length of the gripping zone is designed to be 40 mm. The tabs are cut from .125" (3.175 mm) thick glass epoxy panels, and glued by J-B Weld® Professional two-part epoxy system. To ensure strong bonding, the contacting surfaces of the gripping zone and the tabs are sanded before gluing. The notches are cut by the same saw as the one used to cut SENT coupons. Because the fibers are much tougher than the matrix, the extra damage is not a big concern for DENT coupons. Fig. 3.12 is a photo of a DENT coupon with glass epoxy tabs and notches.

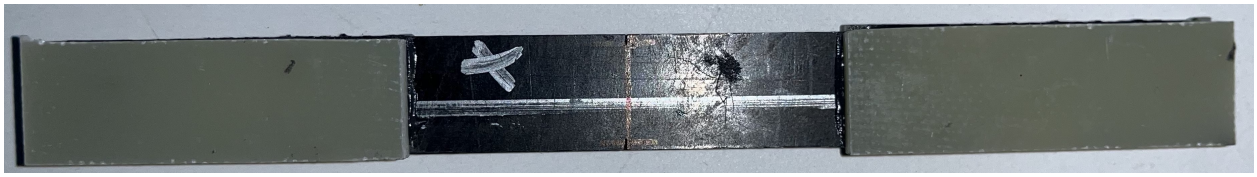

Figure 3.12: A small-sized DENT coupon with tabs and notches

3.3.3 DCB Tests of IM7/977-3 0UD Laminates

DCB tests of IM7/977-3 0-Degree UniDirectional (0UD) laminates are conducted to examine the fiber-dominated Mode I intralaminar fracture of IM7/977-3 laminates. To create a notch between plies, a piece of 0.0005" (12.7 μm) Teflon sheet is inserted in the middle laid up

plies, as described in the previous section.

The ASTM D5528 handbook specifies the dimensions in detail, as shown in Fig. 3.13. Table. 3.5 lists the dimensions of the three sizes of DCB coupons being tested.

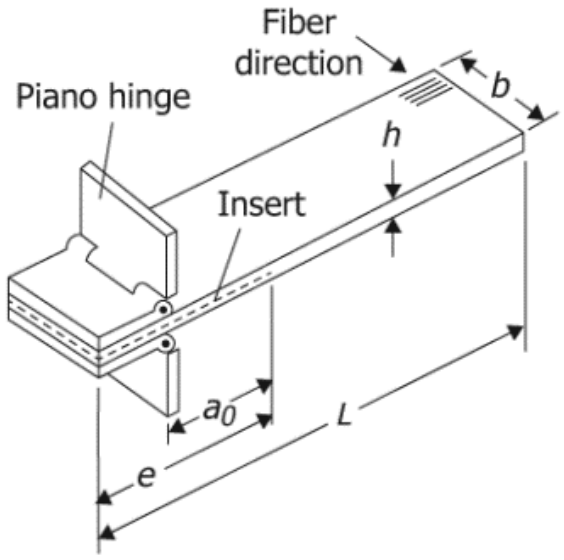

Figure 3.13: Schematics of DCB coupons [5]

Size	L (mm)	e (mm)	h (mm)	$AR = (L-e)/h$	a_0	$\alpha_0 = a_0/(L-e)$	b (mm)
S	125	25	1.12	89.29	40	0.4	25
M	225	25	2.24	89.29	80	0.4	25
L	425	25	4.48	89.29	160	0.4	25

Table 3.5: Designated Dimensions of DCB Coupons

The thicknesses of the coupons are controlled by the number of plies. The number of plies used in small-, medium- and large-sized coupons are 8, 16, and 32 respectively, and the theoretical thicknesses of coupons are calculated by multiplying the number of plies by the thickness of a single ply, which is 0.14 mm. However, due to the surface roughness and

the epoxy squeezing out from the prepreg under pressure, the measured thickness can differ from the theoretical one.

The piano hinges used in the test are glued on the end of the DCB coupons by J-B Weld® Professional two-part epoxy system. To ensure bonding strength, the ends of DCB coupons are sanded prior to gluing.

From the research done by Howe, the thickness of the Teflon sheet can greatly affect the results of interlaminar fracture tests. Howe found that the thicker Teflon sheet (76 μm in his research) creates a large resin pocket ahead of the Teflon sheet front, and increases the notch radius, resulting in the reduction of the stress concentration at the notch tip. To mitigate the influence of resin pocket and crack radius, Howe suggested a Teflon sheet with a thickness of less than 13 μm. Therefore, the 0.0005" thick Teflon sheets are used in this study, following Howe's suggestion. [15]

To study the strain localization near the crack tip, a Digital Image Correlation (DIC) pattern is applied to one of the DCB coupons. To apply the DIC pattern, a layer of white paint is first applied on the side of the chosen DCB coupon, and black paint speckles are randomly applied above the white paint layer. The randomness of the speckles ensures the quality of the DIC analysis.

3.3.4 ENF of IM7/977-3 0UD Laminates

ENF tests of IM7/977-3 0UD laminates are conducted to examine the fiber-dominated Mode II intralaminar fracture of IM7/977-3 laminates. The interlaminar cracks of ENF coupons are created by the same method as the one being used on DCB coupons.

The ASTM D7905 handbook specifies the dimensions in detail, as shown in Fig. 3.14. Table. 3.6 lists the dimensions of the three sizes of ENF coupons being tested.

DIC analysis is also performed on one of the ENF coupons to study the strain localization near the crack tip. The DIC pattern is applied by the same method as the one used for DCB coupons.

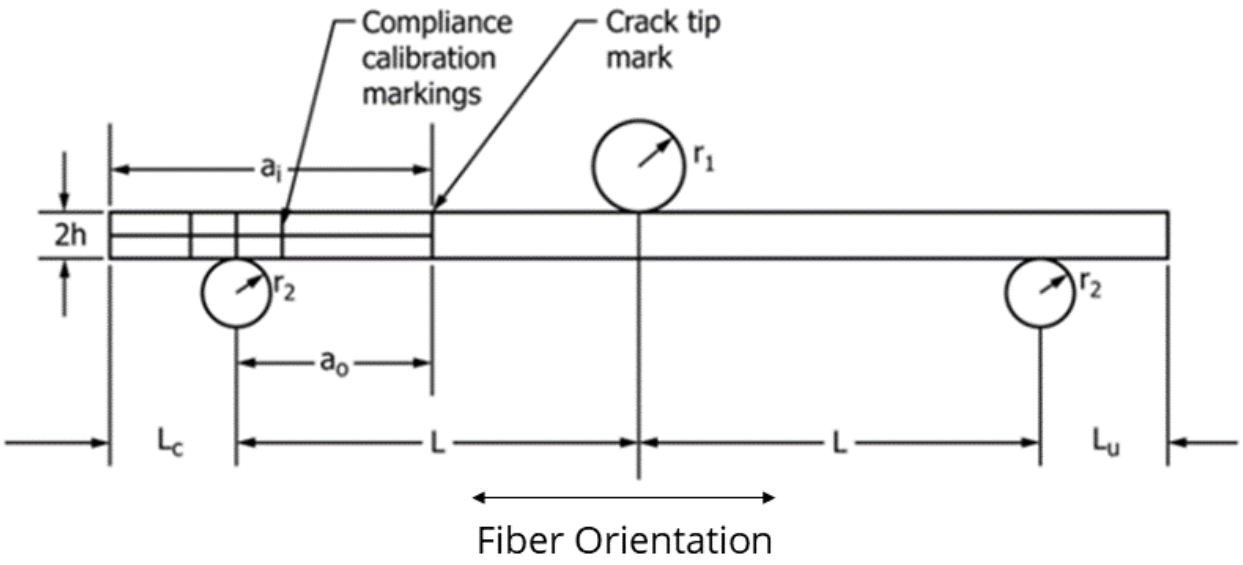

Figure 3.14: Schematics of ENF coupons [4]

Size	L (mm)	L_c&L_u (mm)	$2h$ (mm)	AR=$2L/h$	a_0 (mm)	$\alpha_0 = a_0/2L$	b (mm)
S	36	7.2	1.12	64.29	10.8	0.15	25
M	72	14.4	2.24	64.29	21.6	0.15	25
L	144	28.8	4.48	64.29	43.2	0.15	25

Table 3.6: Designated Dimensions of ENF Coupons

Chapter 4

MODE I MATRIX DOMINATED INTRALAMINAR FRACTURE

This chapter aims to discuss the test results, finite element method simulation, and size-effect analysis of the SENT test of IM7/977-3 $[90]_{12}$ laminates, which is dominated by the Mode I intralaminar fracture of 977-3 matrix. In this study, the dimension variable D is defined as the width of the SENT coupon b.

4.1 Experimental Setup

The SENT test is conducted on the Psylotech μTS load frame (as shown in Fig. 4.1) with a 10 kN load cell. To ensure the gripping quality of the fixture and avoid slippage, the 20 mm gripping zone is marked prior to the test, and a torque wrench with a 20.6 N·m torque setting is used to tighten the clamping bolt on the tension test fixture. While tightening the coupons, the fixture exerts a compressional load on the coupon, so a small number of tensile steps are applied simultaneously to mitigate the compressional load. When the coupons are fully tightened, a 10∼20 N pre-tension is applied to them to mitigate compliance issues due to improper clamping.

The test is set to be displacement controlled with a designated strain rate of 0.05% per minute, so the three sizes are set by different displacement rates, as shown in Table. 4.1. This designated rate ensures that the coupon will fail in 5 minutes while maintaining the quasi-static loading condition. The test stops once the SENT coupon breaks.

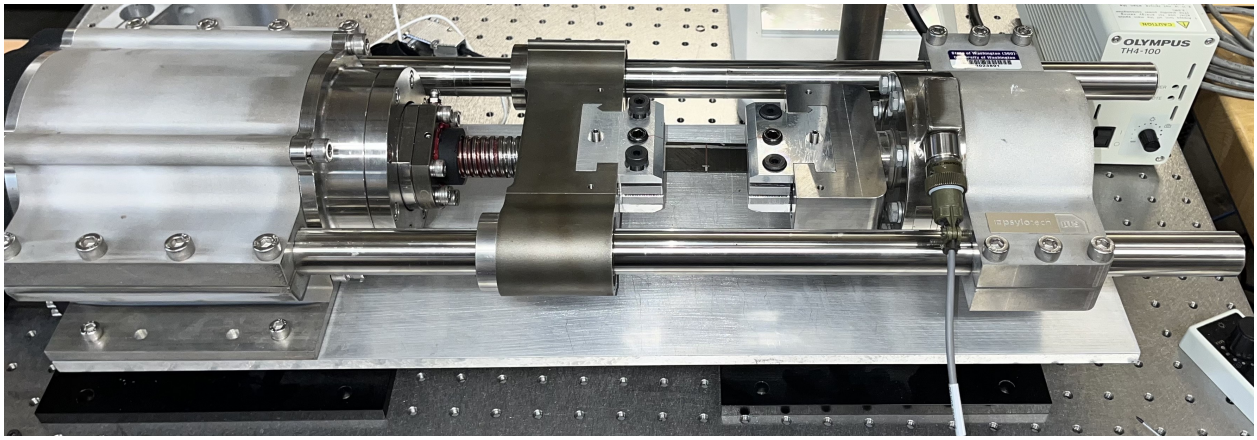

Figure 4.1: A SENT coupon being tested on the Psylotech μTS load frame

Size	D (mm)	$\dot{u}$ (μm/min)	$\dot{\epsilon}$ (min^{-1})
S	12.5	12.5	0.05%
M	25	25	0.05%
L	50	50	0.05%

Table 4.1: The displacement control setting of SENT test

4.2 Test Results

The results of SENT tests are displayed in Table. 4.2 and Fig. 4.2. The crack propagated from the initial crack is perfectly perpendicular to the direction of loading, as shown in Fig. 4.3. Due to the variation in the coupon dimensions and extra damage at the crack tip, discrepancies in fracture loads are observed. And because of the slippage, some of the load-displacement curves do not have fully linear behavior, but since the fracture mechanics size effect study focuses on the structural fracture at the maximum load, which is not affected by slippage, the data from such coupons are still usable.

Size	D (mm)	Number of Coupons Tested	Mean Fracture Load (N)	Coefficient of Variation %
S	12.5	3	374.7	3.53
M	25	5	558.8	10.24
L	50	4	835.2	8.38

Table 4.2: Fracture load of SENT coupons

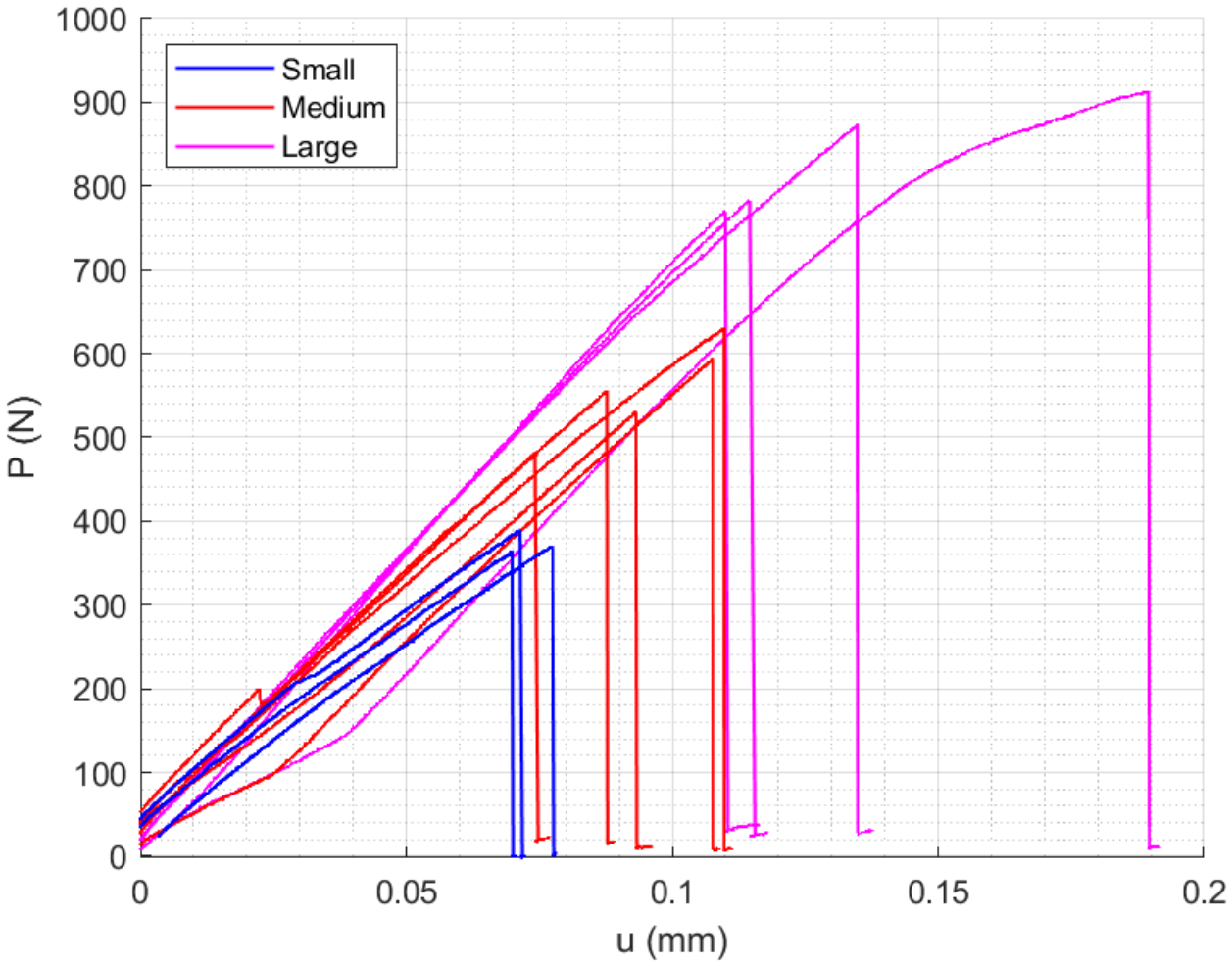

Figure 4.2: The load-displacement curves of SENT coupons of three sizes

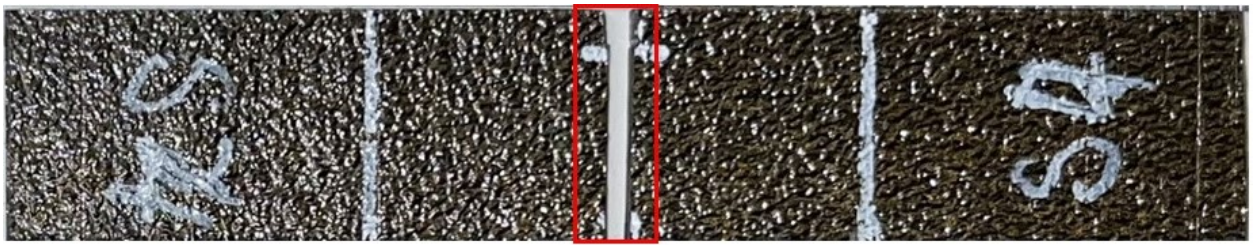

Figure 4.3: The photo of a tested small-sized SENT coupon, showing regular and crack in the middle of the coupon

4.3 Finite Element Method Simulation

In order to perform a linear regression of the test data based on Eq. 2.13, the first step is to determine the dimensionless energy release rate $g(\alpha_0)$ and its derivative $g'(\alpha_0)$ according to Eq. 2.11 and 2.12. Therefore, four quantities including the dimension variable D, the nominal stress at fracture σ_{Nc}, the effective stiffness E', and the energy release rate G need to be defined or calculated to determine $g(\alpha_0)$ and $g'(\alpha_0)$.

The dimension variable D of the SENT test is defined to be the width of the coupon b, and the nominal stress at fracture σ_{Nc} is defined as

$$\sigma_{Nc} = \frac{P}{bh} \tag{4.1}$$

The effective stiffness E' is defined as the stiffness in the direction of loading. In this case, since the laminate is 90-degree unidirectional, E' can be simply treated as $E_{2T} = 8.98$ GPa.

Due to the effect of FPZ, the energy release rate G cannot be determined by LEFM, and the J-integral method based on finite element analysis (FEA) is one of the best choices in this situation. The finite element analysis software Abaqus is used in this study.

The SENT coupon, excluding the gripping zone, is modeled in Abaqus. The designated crack tip and crack seam are defined at the middle of the top edge. To simulate the experimental tensile test, a fixed-end boundary condition is set on the left edge of the coupon, and a uniform horizontal displacement of 1mm is set on the right edge, as shown in Fig. 4.4 (coupling constraints are used on both edges, so the reference points can represent the

displacement and load of the entire edge).

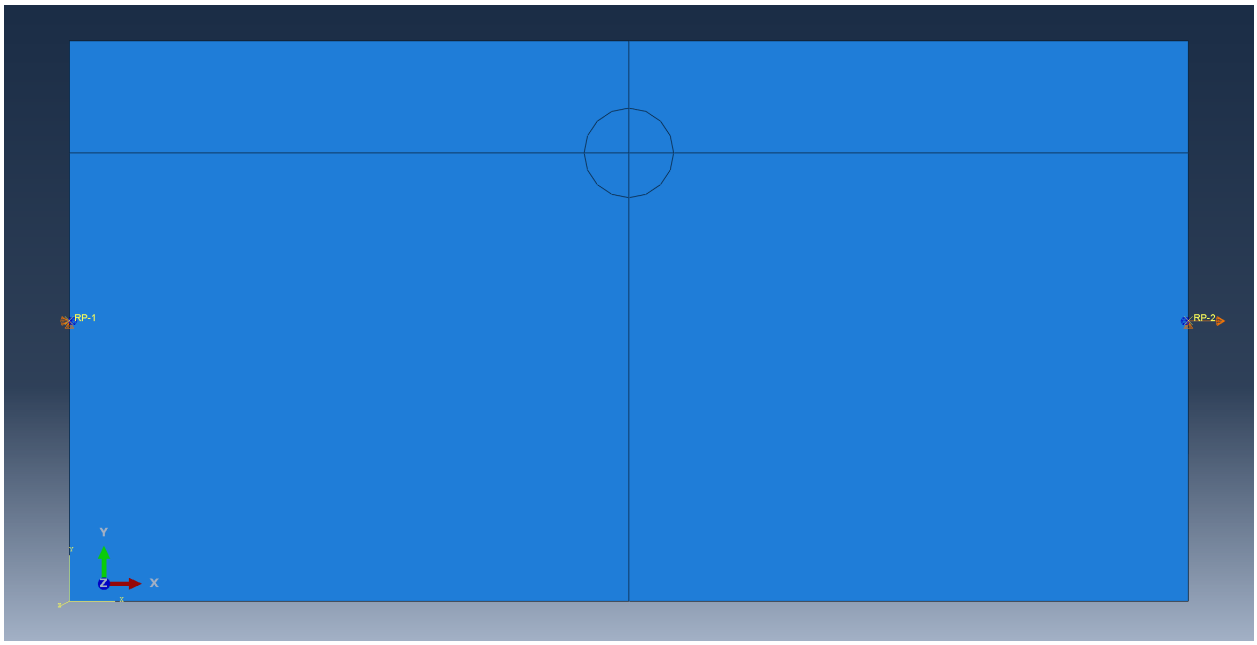

Figure 4.4: The boundary condition setting of Abaqus simulation of SENT coupons

The laminate is modeled as a linear elastic transversely isotropic homogeneous material with the properties shown in Table. 4.3.

E_1 (GPa)	E_2&E_3 (GPa)	G_{12}&G_{13} (GPa)	G_{23} (GPa)	ν_{12}&ν_{13}	ν_{23}
164	8.98	5.01	3.326	0.320	0.350

Table 4.3: Material properties used in Abaqus simulation of SENT coupons

where the in-plane properties are consistent with Table. 3.1 and the out-of-plane Poisson's ratio ν_{23} is estimated using the fact that Poisson's ratio of cured epoxy is usually around 0.35. The out-of-plane shear modulus G_{23} is estimated by

$$G_{23} = \frac{E_2}{2(1+\nu_{23})} \tag{4.2}$$

A quad-dominated, sweep mesh is applied in the circular zone around the crack tip, and a quad, free mesh is applied in the other regions. Because the thickness of the SENT coupons is much smaller than its width, the plane stress quadratic element CPS8 is set. Fig. 4.5 displays the meshing setting of SENT coupons. A quarter-node element at the crack tip is used to simulate the crack front.

The same boundary condition and meshing settings are used to simulate the SENT coupons with a crack length ratio of $\alpha_0 \pm \Delta\alpha$ where $\Delta\alpha = 0.005\alpha_0$. Table. 4.4 and 4.5 conclude all the computed J-integral, the reaction force, and $g(\alpha_0)$ and $g'(\alpha_0)$ determined from Eq. 2.11 and 2.12.

Size	D (mm)	$J(\alpha_0)$ (N/mm)	$P(\alpha_0)$ (kN)	$g(\alpha_0)$
S	12.5	103.9	7.12	0.650
M	25	51.9	7.12	0.650
L	50	26.0	7.12	0.650

Table 4.4: The J-integrals, reaction forces, and dimensionless energy release rate of SENT coupons with $\alpha_0 = 0.2$

Size	D (mm)	$J(\alpha_0 - \Delta\alpha)$ (N/mm)	$J(\alpha_0 + \Delta\alpha)$ (N/mm)	$P(\alpha_0 - \Delta\alpha)$ (kN)	$P(\alpha_0 + \Delta\alpha)$ (kN)	$g'(\alpha_0)$
S	12.5	103.4	104.4	7.12	7.11	4.07
M	25	51.7	52.2	7.12	7.11	4.07
L	50	25.8	26.1	7.12	7.11	4.07

Table 4.5: The J-integrals and reaction forces of SENT coupons with $\alpha_0 \pm \Delta\alpha$ and the computed dimensionless energy release rate gradient

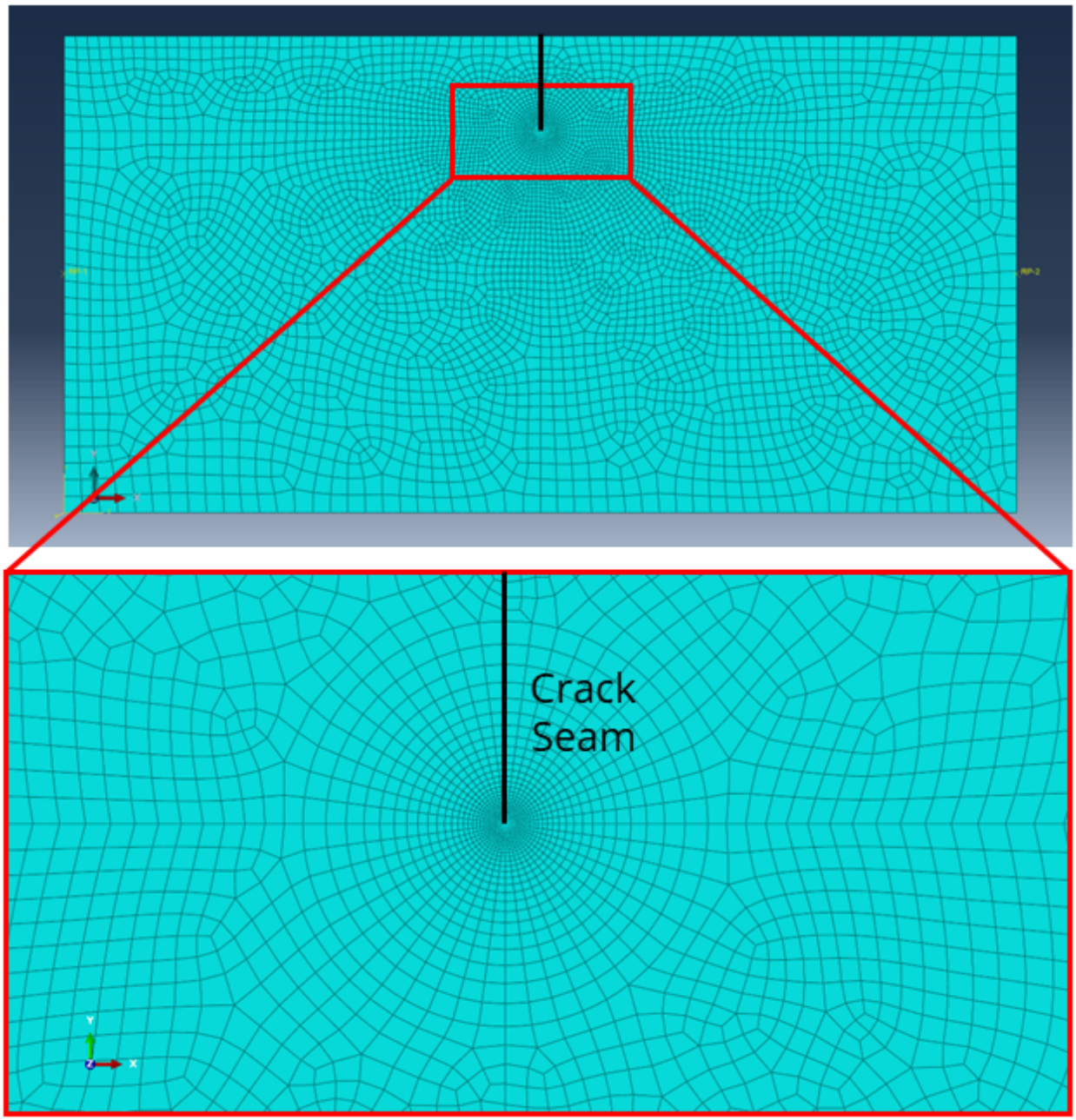

Figure 4.5: The meshing setting of Abaqus simulation of SENT coupons

4.4 Analysis

Due to the existence of FPZ in the IM7/977-d laminate, the fracture load of three sizes of coupon deviates from the trend of LEFM, and the SEL must be utilized to account for the

influence of FPZ. According to Eq. 2.13, a weighted linear regression is performed to find out the coefficients A and B. The weight of each data point is designated so that the sum of the weight of the data points of the same size is exactly 1/3. For example, if there are 4 small-sized SENT coupons tested, then the weight of each data point of a small-sized coupon is 1/12. The weight ensures an equal influence of each size on the linear regression result.

The linear regression result of the SENT test is displayed in Fig. 4.6 and Table. 4.6. The curve fit is not perfect because of the variation of the data mainly due to the extra damage.

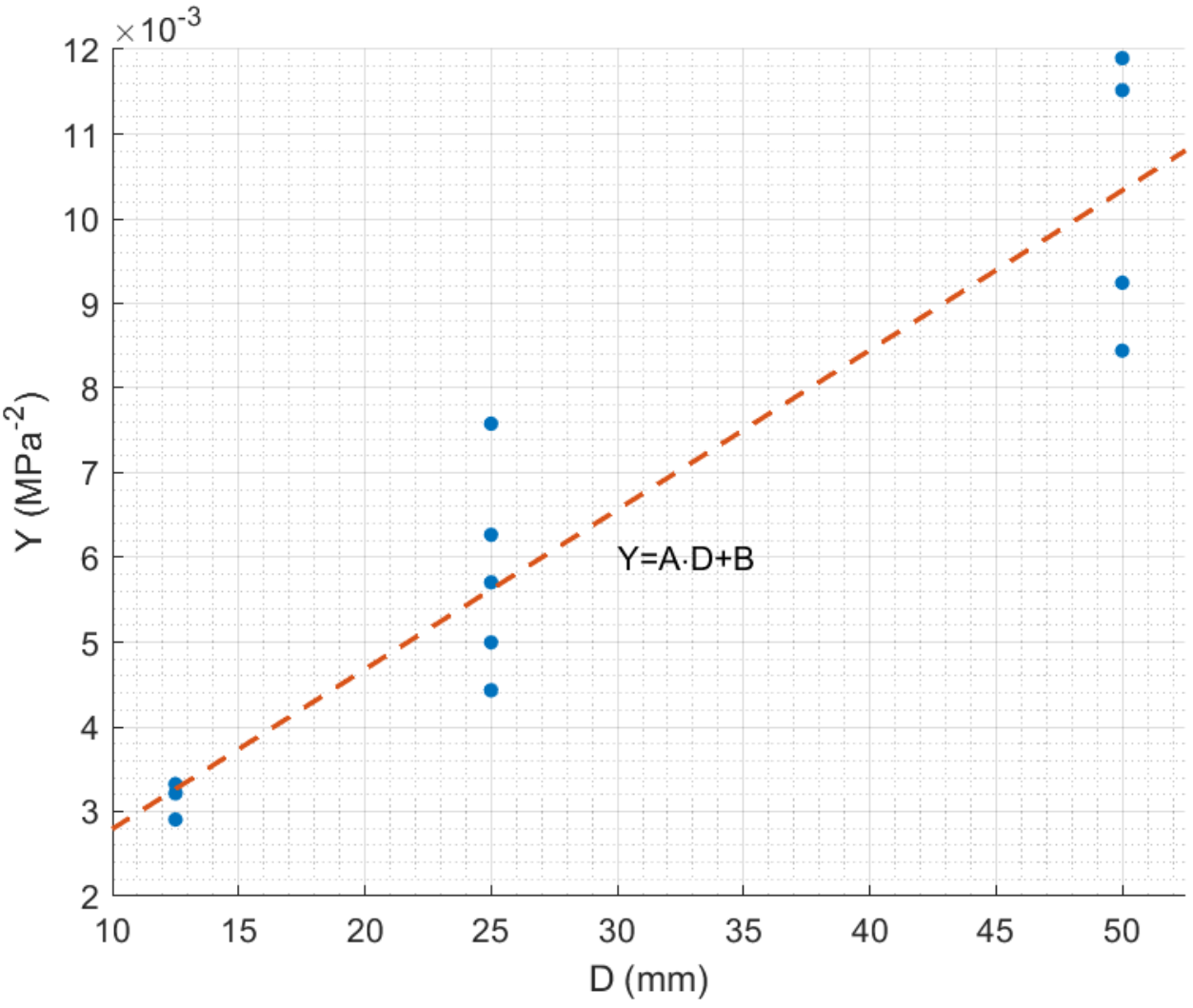

Figure 4.6: The linear regression of SENT test results based on Eq. 2.13

A (MPa^{-2}mm^{-1})	B (MPa^{-2})	R^2
1.88×10^{-4}	9.10×10^{-4}	0.884

Table 4.6: The linear regression of SENT test results based on Eq. 2.13

Table. 4.7 shows the key size effect parameters determined by Eq. 2.14, 2.15, 2.16 and 2.17. Based on the determined properties, the SEL curve fit is plotted to show demonstrate the influence of FPZ, as shown in Fig. 4.7, and the brittleness of SENT coupons is computed and displayed in Table. 4.8.

G_{Ic} (N/mm)	C_f (mm)	σ_0 (MPa)	D_0 (mm)
0.384	0.770	33.2	4.83

Table 4.7: Key size effect parameters of matrix-dominated intralaminar Mode I fracture of IM7/977-3 $[90]_{12}$ laminates

Size	D (mm)	β	LEFM Prediction (MPa)	SEL Prediction (MPa)	Error %
S	12.5	2.59	20.6	17.5	+17.73
M	25	5.18	14.6	13.3	+9.23
L	50	10.36	10.3	9.8	+4.72

Table 4.8: Brittleness of SENT coupons and the comparison between LFEM and SEL predictions

Based on the size effect law curve and the brittleness table, it can be concluded that starting from the medium-size coupons, the nominal stress deviates from the LEFM trend, and LEFM tends to overestimate the fracture load. Therefore, the LEFM trend cannot be directly applied on the 90-degree unidirectional IM7/977-3 laminates with a width of less than 50 mm, and reckless application of LEFM is fatal due to overestimation.

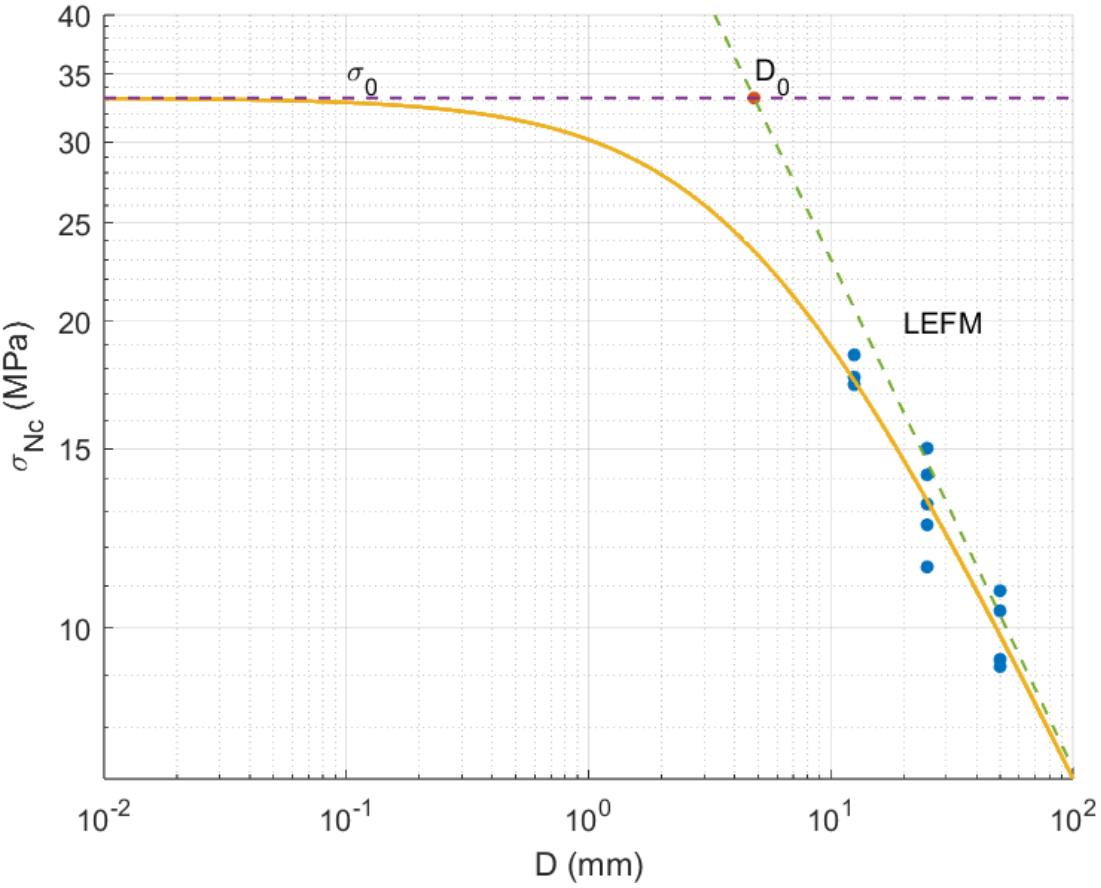

Figure 4.7: The Bažant size effect law curve of matrix-dominated intralaminar Mode I fracture of IM7/977-3 $[90]_{12}$ laminates

Chapter 5

MODE I FIBER-DOMINATED INTRALAMINAR FRACTURE

This chapter aims to discuss the test results, finite element method simulation, and size-effect analysis of the IM7/977-3 $[0/90_5]_s$ laminate DENT test, which is dominated by the Mode I intralaminar fracture of IM7-fiber. In this study, the dimension variable D is defined as the width of the DENT coupon b.

5.1 Experimental Setup

The DENT test is conducted on the Shore Western 306.4 load frame (as shown in Fig. 5.1) with a 100 kip load cell. As discussed in the previous chapter, the 40 mm gripping zones of the DENT coupons are covered by 0.125" thick glass epoxy tabs to prevent laminate crushing. The hydraulic-driven gripping fixture provides sufficient gripping force to prevent slippage. A pre-tensile load of $\sim$ 0.2 kN is used to ensure good gripping and mitigate compliance.

The test is set to be displacement controlled with a designated strain rate of 0.2% per minute, so the three sizes are set by different displacement rates, as shown in Table. 5.1. This designated rate ensures that the coupon will fail in 5 minutes while maintaining the quasi-static loading condition. The test stops once the DENT coupon breaks.

Size	D (mm)	$\dot{u}$ (mm/min)	$\dot{\epsilon}$ (min^{-1})
S	12.5	0.1	0.2%
M	25	0.2	0.2%
L	50	0.4	0.2%

Table 5.1: The displacement control setting of DENT test

Figure 5.1: (a) Shore Western 306 Series load frame; (b) A DENT coupon being tested

5.2 Test Results

The results of DENT tests are displayed in Table. 5.2 and Fig. 5.2. The distribution of fracture load is due to two major reasons. The first reason is the variation in coupon geometry, and the more important reason is the extra modes of energy dissipation. Although 10 layers of 90-degree plies are included between the two 0-degree plies, and both edges of the coupon are notched, as discussed in the previous chapter, the crack created by fiber breakage is still not perfect and involves irregular geometry and fiber detachment from the

laminate, as shown in Fig. 5.3, and the irregularity of the crack and the amount of fiber detached varies from coupon to coupon. However, the distribution is still acceptable, and a statistical size effect study can still be conducted.

Size	D (mm)	Number of Coupons Tested	Mean Fracture Load (kN)	Coefficient of Variation %
S	12.5	5	7.80	8.69
M	25	5	13.45	3.62
L	50	5	25.63	9.21

Table 5.2: Fracture load of DENT coupons

5.3 Finite Element Method Simulation

The Abaqus-assisted J-integral method is also used to determine g and g' for DENT coupons. In this test, D is defined as the width of the coupon, and the nominal stress is defined as

$$\sigma_{Nc} = \frac{P}{bh} \tag{5.1}$$

Since the DENT coupon is not unidirectional, CLT must be utilized to model the coupon as a linear elastic orthotropic homogeneous material. First, the "ABD" matrix of IM7/977-3 $[0/90_5]_s$ laminate is computed and then inversed to get the "abd" matrix:

$$\begin{bmatrix} A_{11} & A_{12} & A_{16} & B_{11} & B_{12} & B_{16} \\ A_{12} & A_{22} & A_{26} & B_{12} & B_{22} & B_{26} \\ A_{16} & A_{26} & A_{66} & B_{16} & B_{26} & B_{66} \\ B_{11} & B_{12} & B_{16} & D_{11} & D_{12} & D_{16} \\ B_{12} & B_{22} & B_{26} & D_{12} & D_{22} & D_{26} \\ B_{16} & B_{26} & B_{66} & D_{16} & D_{26} & D_{66} \end{bmatrix}^{-1} = \begin{bmatrix} a_{11} & a_{12} & a_{16} & b_{11} & b_{12} & b_{16} \\ a_{12} & a_{22} & a_{26} & b_{12} & b_{22} & b_{26} \\ a_{16} & a_{26} & a_{66} & b_{16} & b_{26} & b_{66} \\ b_{11} & b_{12} & b_{16} & d_{11} & d_{12} & d_{16} \\ b_{12} & b_{22} & b_{26} & d_{12} & d_{22} & d_{26} \\ b_{16} & b_{26} & b_{66} & d_{16} & d_{26} & d_{66} \end{bmatrix} \tag{5.2}$$

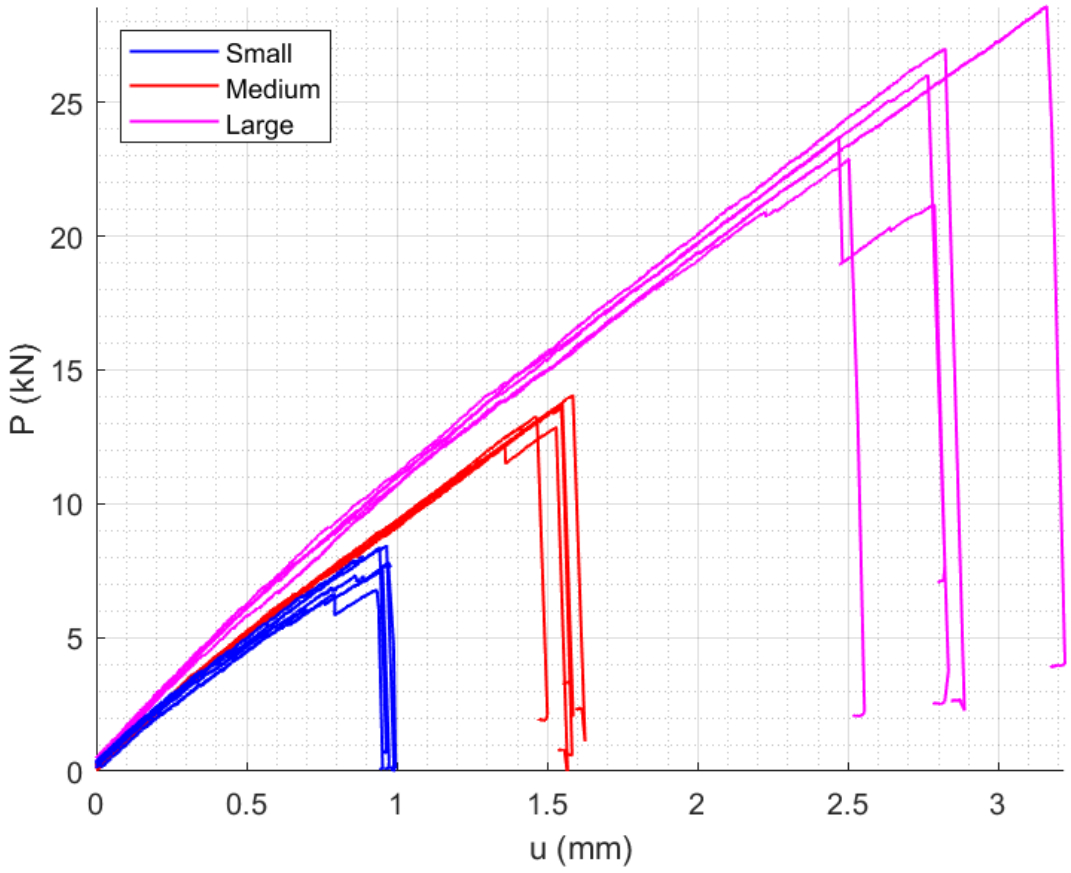

Figure 5.2: The load-displacement curves of DENT coupons of three sizes

Figure 5.3: A DENT coupon after the test. The crack is irregular and fiber splitting significantly contributes to energy dissipation.

Based on the "abd" matrix, the in-plane effective modulus and Poisson's ratio of the cross-ply laminate can be calculated by:

$$E_1' = \frac{1}{ha_{11}} \tag{5.3}$$

$$E_2' = \frac{1}{ha_{22}} \tag{5.4}$$

$$G_{12}' = \frac{1}{ha_{66}} \tag{5.5}$$

$$\nu_{12}' = -\frac{a_{12}}{a_{11}} \tag{5.6}$$

and the out-plane properties can be estimated based on the series rule:

$$G_{13}' = \frac{2}{12}G_{13} + \frac{10}{12}G_{23} \tag{5.7}$$

$$G_{23}' = \frac{10}{12}G_{13} + \frac{2}{12}G_{23} \tag{5.8}$$

$$\nu_{13}' = \frac{2}{12}\nu_{13} + \frac{10}{12}\nu_{23} \tag{5.9}$$

$$\nu_{23}' = \frac{10}{12}\nu_{13} + \frac{2}{12}\nu_{23} \tag{5.10}$$

$$E_3' = E_3 \tag{5.11}$$

Table. 5.3 lists the properties of equivalent homogeneous material used in Abaqus simulation.

E_1' (GPa)	E_2' (GPa)	E_3' (GPa)	G_{12}' (GPa)	G_{13}' (GPa)	G_{23}' (GPa)	ν_{12}'	ν_{13}'	ν_{23}'
34.95	138.7	8.98	5.01	3.606	4.729	0.0208	0.345	0.325

Table 5.3: Material properties used in Abaqus simulation of DENT coupons

The effective stiffness E' is defined as the stiffness in the direction of loading. In this case, since the laminate is 90-degree unidirectional, E' is treated as $E_1' = 34.95$ GPa.

The half-DENT coupon, excluding the gripping zone, is modeled in Abaqus. The designated crack tip and crack seam are defined at the middle of the top edge, and mirror symmetry is applied on the bottom edge. To simulate the experimental tensile test, a fixed-end boundary condition is set on the left edge of the coupon, and a uniform horizontal displacement of 1mm is set on the right edge, as shown in Fig. 4.4 (coupling constraints are used on both edges, so the reference points can represent the displacement and load of the half-edge). A similar meshing strategy to the one used in the SENT simulation is applied to the DENT model. The settings of boundary condition setting and meshing of the DENT coupon are demonstrated in Fig. 5.4 and Fig. 5.5.

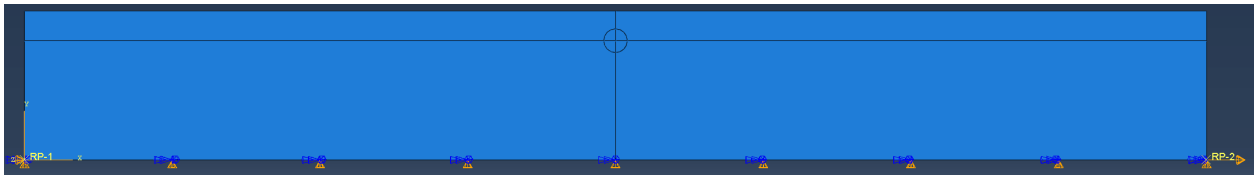

Figure 5.4: The boundary condition setting of Abaqus simulation of DENT coupons

Since only half of the coupon is modeled, the J-integral and load determined by Abaqus are halved. Table. 5.4 and 5.5 conclude all the computed J-integral, the reaction force, and $g(\alpha_0)$ and $g'(\alpha_0)$ determined from Eq. 2.11 and 2.12.

Size	D (mm)	$J(\alpha_0)/2$ (N/mm)	$P(\alpha_0)/2$ (kN)	$g(\alpha_0)$
S	12.5	80.4	7.17	0.965
M	25	40.2	7.17	0.965
L	50	20.1	7.17	0.965

Table 5.4: The J-integrals, reaction forces, and dimensionless energy release rate of DENT coupons with $\alpha_0 = 0.2$

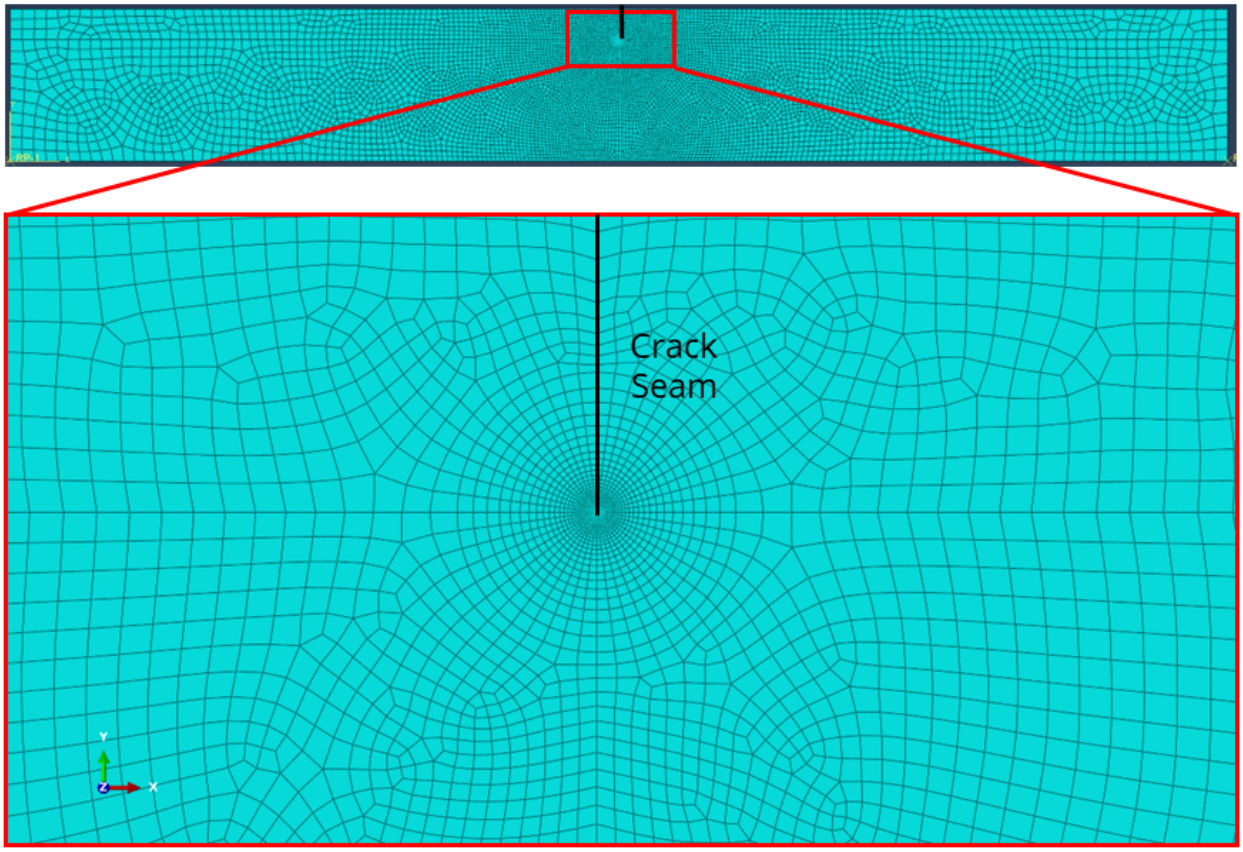

Figure 5.5: The meshing setting of Abaqus simulation of DENT coupons

Size	D (mm)	$J(\alpha_0 - \Delta\alpha)/2$ (N/mm)	$J(\alpha_0 + \Delta\alpha)/2$ (N/mm)	$P(\alpha_0 - \Delta\alpha)/2$ (kN)	$P(\alpha_0 + \Delta\alpha)/2$ (kN)	$g'(\alpha_0)$
S	12.5	80.0	80.8	7.17	7.17	4.96
M	25	40.0	40.4	7.17	7.17	4.96
L	50	20.0	20.2	7.17	7.17	4.96

Table 5.5: The J-integrals and reaction forces of DENT coupons with $\alpha_0 \pm \Delta\alpha$ and the computed dimensionless energy release rate gradient

5.4 Analysis

The analysis of DENT tests uses the same weighted linear regression method that is used for SENT tests. The linear regression result of the DENT test is displayed in Fig. 5.6 and

Tab. 5.6. The curve fit is far from perfect because of the significant contribution of extra modes of energy dissipation, such as fiber detachment.

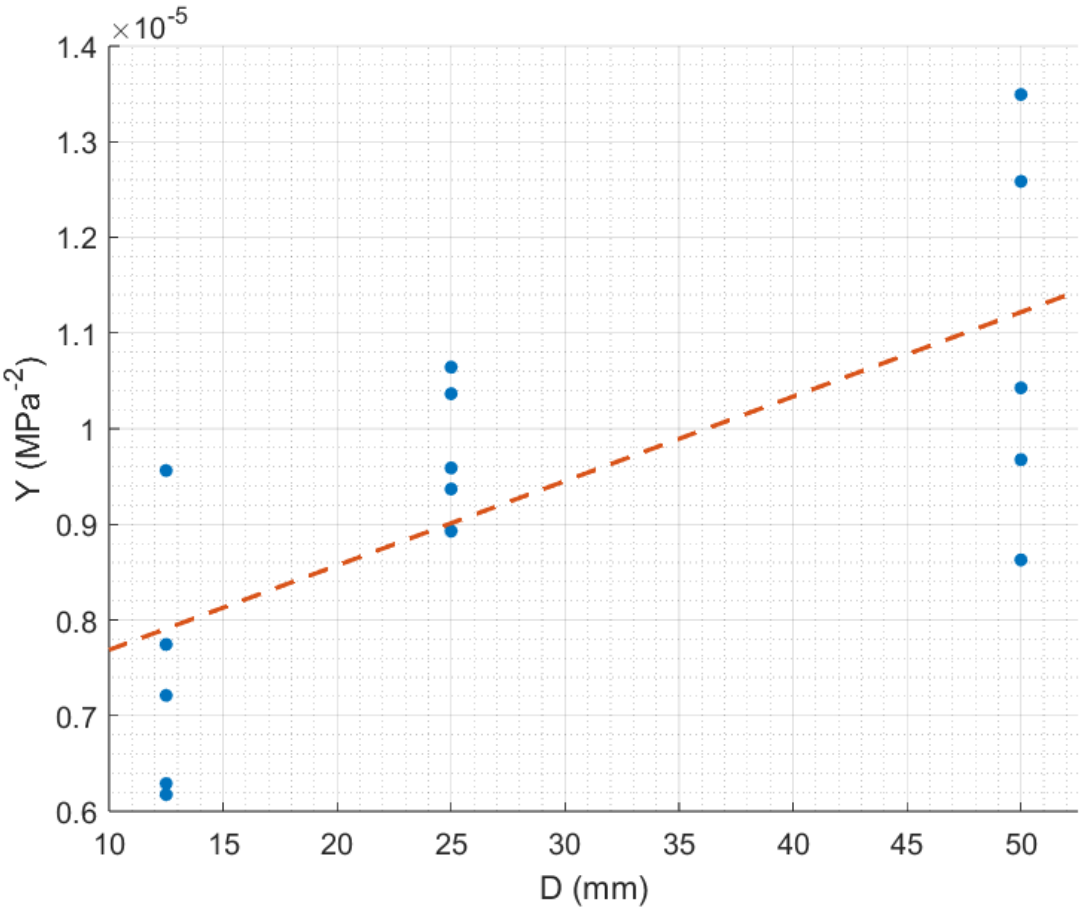

Figure 5.6: The linear regression of DENT test results based on Eq. 2.13

A (MPa^{-2}mm^{-1})	B (MPa^{-2})	R^2
8.83×10^{-8}	6.80×10^{-6}	0.481

Table 5.6: The linear regression of DENT test results based on Eq. 2.13

However, although the quality of the linear regression is relatively low, it still shows that

the DENT test results still significantly deviate from the LEFM trend. Table. 5.6 shows the key size effect parameters determined by Eq. 2.14, 2.15, 2.16 and 2.17. Because in the previous chapter, the fracture energy of 90-unidirectional laminate is 0.38395 N/mm, which is far less than the fracture energy of cross-ply laminates, the two 0-degree plies contribute most of the fracture energy. Therefore, the fracture energy of 0-degree unidirectional plies is approximately 6 times the fracture energy of $[0/90_5]_s$ cross-ply laminates, $G_{Ic} \sim 2000$ N/mm.

G_{Ic} (N/mm)	C_f (mm)	σ_0 (MPa)	D_0 (mm)
313	15.0	383	77.1

Table 5.7: Key size effect parameters of fiber-dominated intralaminar Mode I fracture of IM7/977-3 $[0/90_5]_s$ laminates

Based on the determined properties, the SEL curve fit is plotted to show demonstrate the influence of FPZ, as shown in Fig. 5.7, and the brittleness of DENT coupons is computed and displayed in Table. 5.8.

Size	D (mm)	β	LEFM Prediction (MPa)	SEL Prediction (MPa)	Error %
S	12.5	0.162	952	356	+ 167.7
M	25	0.324	673	333	+102.1
L	50	0.649	476	299	+59.4

Table 5.8: Brittleness of DENT coupons and the comparison between LFEM and SEL predictions

Based on the size effect law curve and the brittleness table, it can be concluded that all three sizes of DENT coupons are within the transition zone between the perfectly ductile and perfectly brittle materials since the effective FPZ length is comparable to the coupon sizes, and LEFM greatly overestimates the results. For cross-ply laminates with a width of

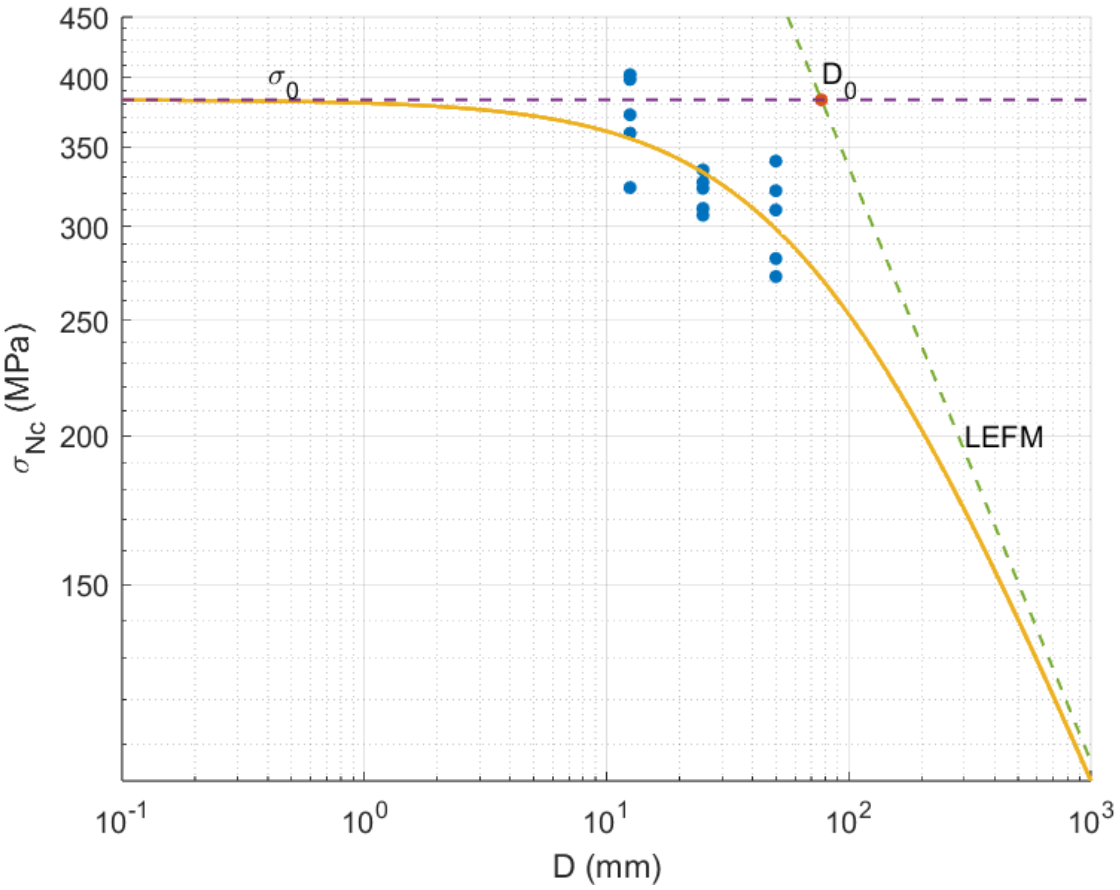

Figure 5.7: The Bažant size effect law curve of fiber-dominated intralaminar Mode I fracture of IM7/977-3 $[0/90_5]_s$ laminates

less than 1 m, the contribution of FPZ to the fracture load must be carefully considered.

Chapter 6
MODE I INTERLAMINAR FRACTURE

This chapter aims to discuss the test results, finite element method simulation, and size-effect analysis of the DCB test of IM7/977-3 0-degree unidirectional laminates, which is dominated by the Mode I interlaminar fracture. This study defines the dimension variable D as the thickness of the DCB coupon h.

6.1 Experimental Setup

The DCB test is conducted by Instron 5585H load frame with a 2kN load cell, as shown in Fig. 6.1. The piano hinges attached to the DCB coupons are hand-tightened to the tension fixture. Since the load exerted on the DCB coupons is very low, slippage is unlikely. For large-sized coupons, the effect of weight is not negligible, so in order to mitigate the influence of self-weight, the coupon is supported to make sure the reading of the load cell is close to zero prior to testing. However, since the coupon moves with the load frame, self-weight still affects the load reading, especially for the large-sized coupons.

The DCB test is load controlled. The coupons are designed to break between two to ten minutes. This designated time interval saves time but still meets the quasi-static loading condition. The load control setting of the DCB test is displayed in Tab. 6.1.

Size	D (mm)	$\dot{P}$ (N/min)
S	1.12	2
M	2.24	4
L	4.48	8

Table 6.1: The load control setting of DCB test

Figure 6.1: (a) Instron 5585H load frame; (b) A DCB coupon being tested

Besides standard load measurement, the strain field is also analyzed by DIC. A Nikon D5600 DSLR camera with a Nikon AF micro 200 mm lens is set in front of the specimen and 3-second interval photo shooting is used to record the change of the DIC grid pattern on the DCB coupon.

6.2 Test Results

The results of DCB tests are displayed in Table. 6.2 and Fig. 6.2. The load-displacement curve of the DCB coupons showed extremely high consistency. Different from regular brittle, unstable crack propagation, it is observed that the interlaminar Mode I crack propagation of IM7/977-3 is stable. The instant corresponds to the initial crack propagation is the end of the linear part of load-displacement curves, and after this instant, while the crack is growing smoothly, the DCB coupons experience gradual strain softening until the final fracture.

Size	D (mm)	Number of Coupons Tested	Mean Fracture Load (N)	Coefficient of Variation %
S	1.12	4	12.60	2.90
M	2.24	4	16.61	3.42
L	4.48	3	24.48	1.99

Table 6.2: Fracture load of DCB coupons

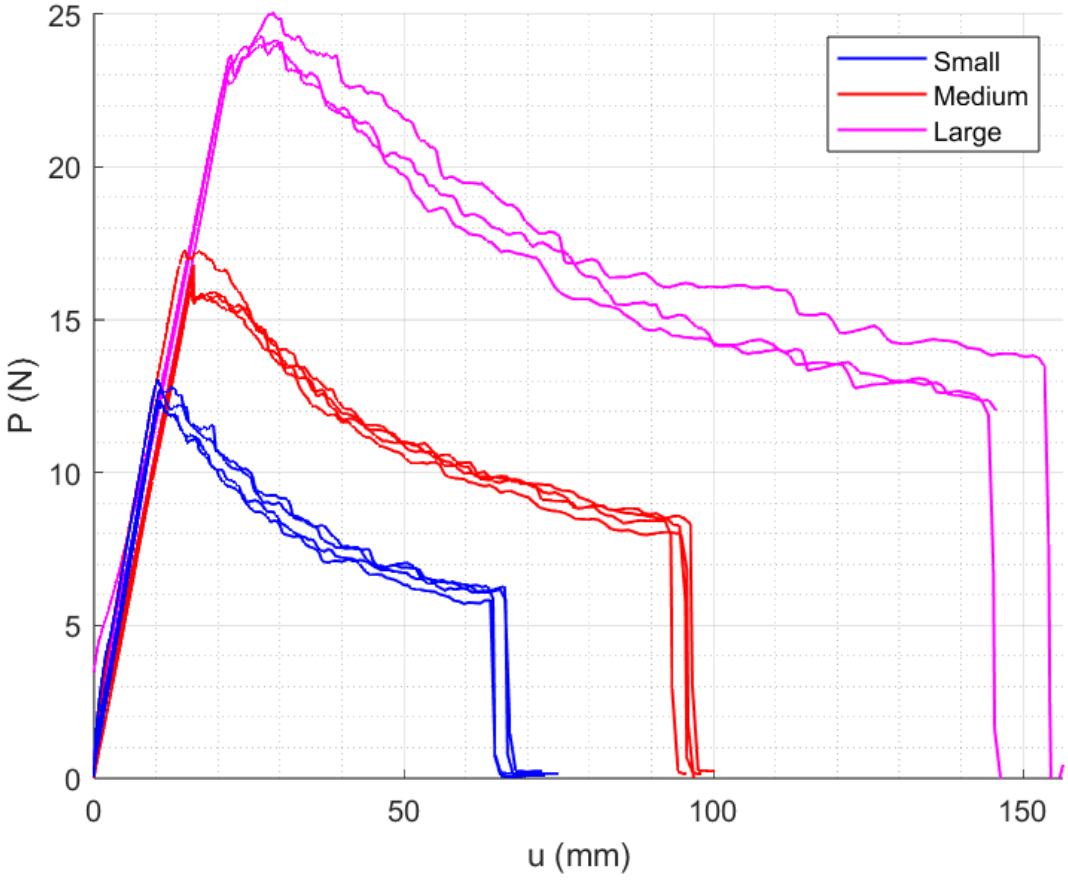

Figure 6.2: The load-displacement curves of DCB coupons of three sizes

The DIC analysis yields the change in the strain field around the crack tip with increasing loading, and Fig. 6.3 displays the 1st principal strain field at the instant just before initial crack propagation, from which significant strain localization is observed in front of the crack tip.

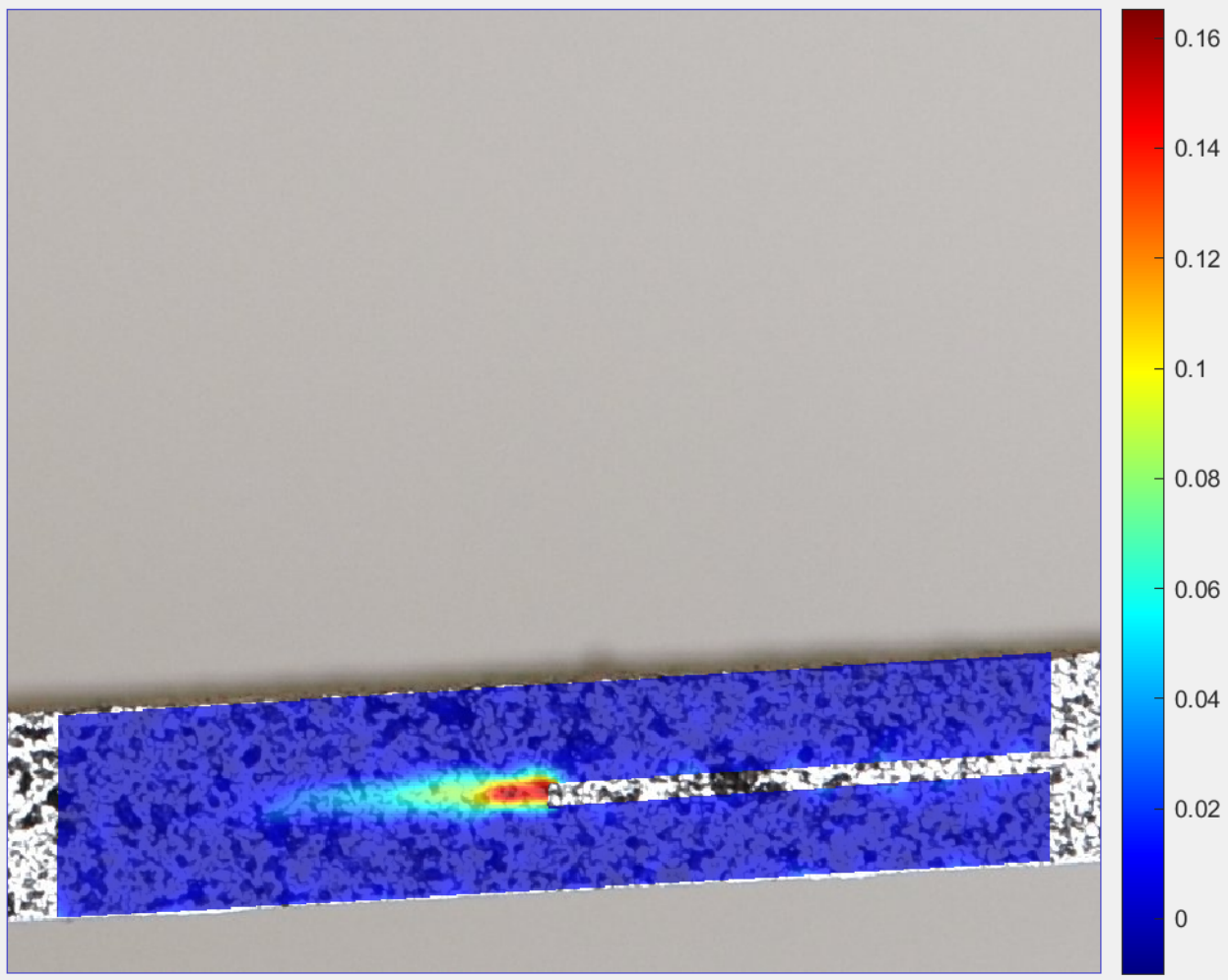

Figure 6.3: The maximum principal strain field around the crack tip of a large-sized DCB coupon

6.3 Finite Element Method Simulation

The Abaqus-assisted J-integral method is also used to determine g and g' for DENT coupons. In this test, D is defined as the thickness of the coupon h, and the nominal stress is defined as

$$\sigma_{Nc} = \frac{P}{bh} \tag{6.1}$$

In this case, the effective stiffness E' is defined as $E' = E_{1T} = 164$ GPa. However, the definition of E' is arbitrary in this case and will not affect the results of the analysis.

The side projection of the DCB coupon excluding the piano hinges is modeled in Abaqus. The designated crack tip and crack seam are defined at the middle of the left edge. To simulate the DCB test, the right edge is set to be zero-translation and zero-rotation, and a uniform vertical displacement of ± 1 mm is set on the top-left corner and top-right corner, as shown in Fig. 6.4.

Figure 6.4: The boundary condition setting of Abaqus simulation of DCB coupons

The laminate is modeled as a linear elastic transversely isotropic homogeneous material with the properties shown in Table. 6.3.

E_1 (GPa)	E_2&E_3 (GPa)	G_{12}&G_{13} (GPa)	G_{23} (GPa)	ν_{12}&ν_{13}	ν_{23}
164	8.98	5.01	3.326	0.320	0.350

Table 6.3: Material properties used in Abaqus simulation of DCB coupons

A sweep, quad-dominated meshing strategy is applied in the circular region around the crack tip, while a free, quad meshing strategy is applied in the rest of the regions. Since the

DCB coupons can be considered thick beams, for which the strain in the width direction is negligible, the plane strain condition can be applied in this case. Therefore, the element type is set to be the plane strain, quadratic CPE8. The mesh of DCB coupons is displayed in Fig. 6.5.

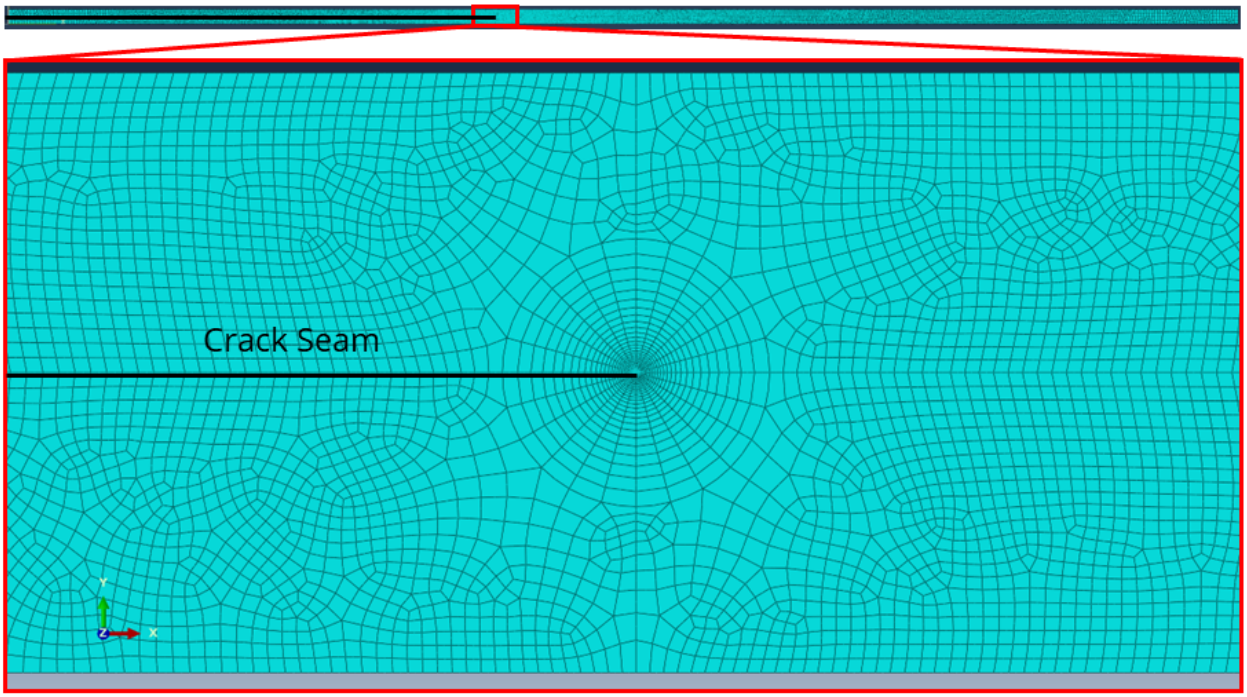

Figure 6.5: The meshing setting of Abaqus simulation of DCB coupons

Table. 6.4 and 6.5 conclude all the computed J-integral, the reaction force, and $g(\alpha_0)$ and $g'(\alpha_0)$ determined from Eq. 2.11 and 2.12.

6.4 Analysis

The weighted linear regression is used for DCB test results as well. The linear regression result of the DCB test is displayed in Fig. 6.6 and Tab. 6.6. The curve fit is nearly perfect, but the y-intersection is quite sensitive to the data, so any additional data may lead to a negative y-intercept. The reason will be discussed in the following.

Size	D (mm)	$J(\alpha_0)$ (N/mm)	$P(\alpha_0)$ (kN)	$g(\alpha_0)$
S	1.12	7.58×10^{-3}	2.60	1.29×10^{5}
M	2.24	3.79×10^{-3}	2.60	1.29×10^{5}
L	4.48	1.90×10^{-3}	2.60	1.29×10^{5}

Table 6.4: The J-integrals, reaction forces, and dimensionless energy release rate of DCB coupons with $\alpha_0 = 0.2$

Size	D (mm)	$J(\alpha_0-\Delta\alpha)$ (N/mm)	$J(\alpha_0+\Delta\alpha)$ (N/mm)	$P(\alpha_0-\Delta\alpha)$ (kN)	$P(\alpha_0+\Delta\alpha)$ (kN)	$g'(\alpha_0)$
S	1.12	7.73×10^{-3}	7.43×10^{-3}	2.64	2.56	6.26×10^{5}
M	2.24	3.86×10^{-3}	3.72×10^{-3}	2.64	2.56	6.26×10^{5}
L	4.48	1.93×10^{-3}	1.86×10^{-3}	2.64	2.56	6.26×10^{5}

Table 6.5: The J-integrals and reaction forces of DCB coupons with $\alpha_0 \pm \Delta\alpha$ and the computed dimensionless energy release rate gradient

A (MPa^{-2}mm^{-1})	B (MPa^{-2})	R^2
4.69	0.167	0.987

Table 6.6: The linear regression of DCB test results based on Eq. 2.13

Tab. 6.7 shows the key size effect parameters determined by Eq. 2.14, 2.15, 2.16 and 2.17. Based on the determined properties, the SEL curve fit is plotted to show demonstrate the influence of FPZ, as shown in Fig. 6.7, and the brittleness of DENT coupons is computed and displayed in Table. 6.8.

Based on the size effect law curve and the brittleness table, it can be concluded that the behavior of DCB coupons is nearly perfectly brittle and linearly elastic. Note that the thickness of the Teflon sheet is 12.7 μm, so the C_f determined by the Bažant size effect

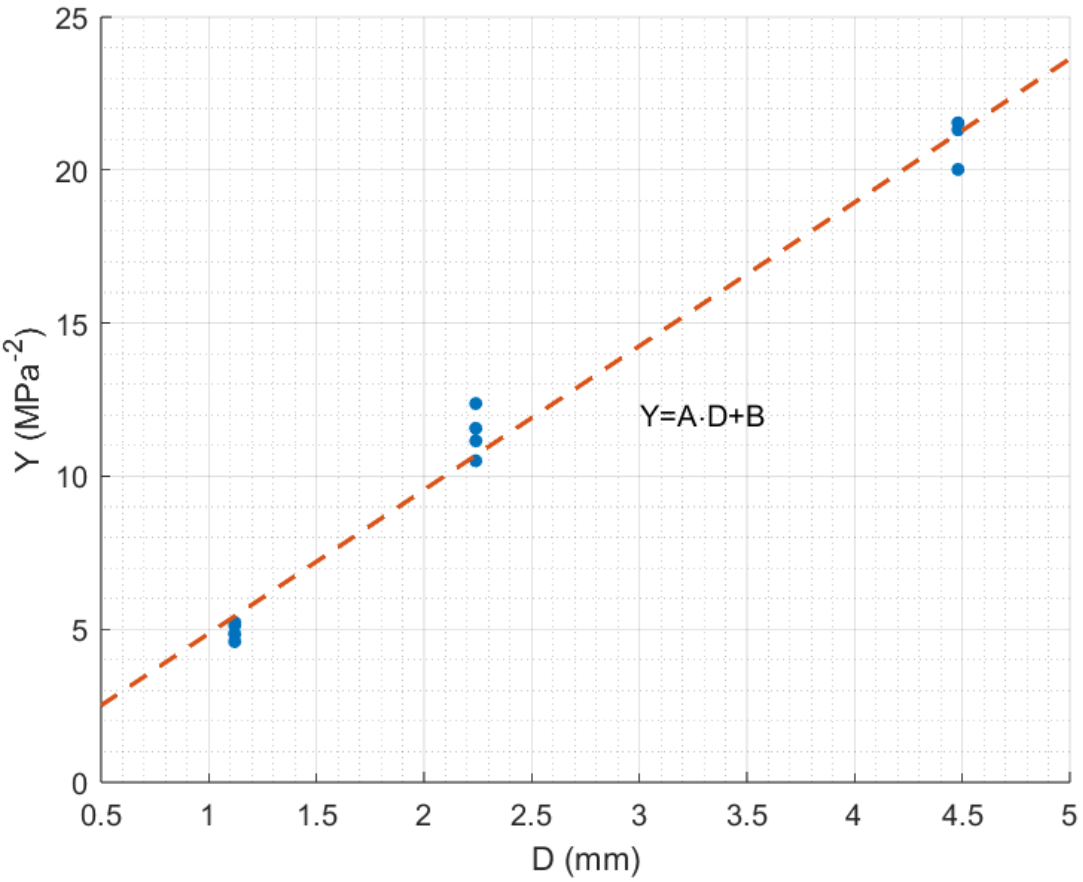

Figure 6.6: The linear regression of DCB test results based on Eq. 2.13

G_{Ic} (N/mm)	C_f (μm)	σ_0 (MPa)	D_0 (μm)
0.167	7.34	2.44	35.7

Table 6.7: Key size effect parameters of interlaminar Mode I fracture of IM7/977-3 0UD laminates

law is less than the crack width, making the C_f value less reliable, but it can still suggest the brittle behavior of DCB coupons. The high brittleness makes the y-intercept very close to zero, and the variation of the fracture loads can lead to a slightly negative y-intercept.

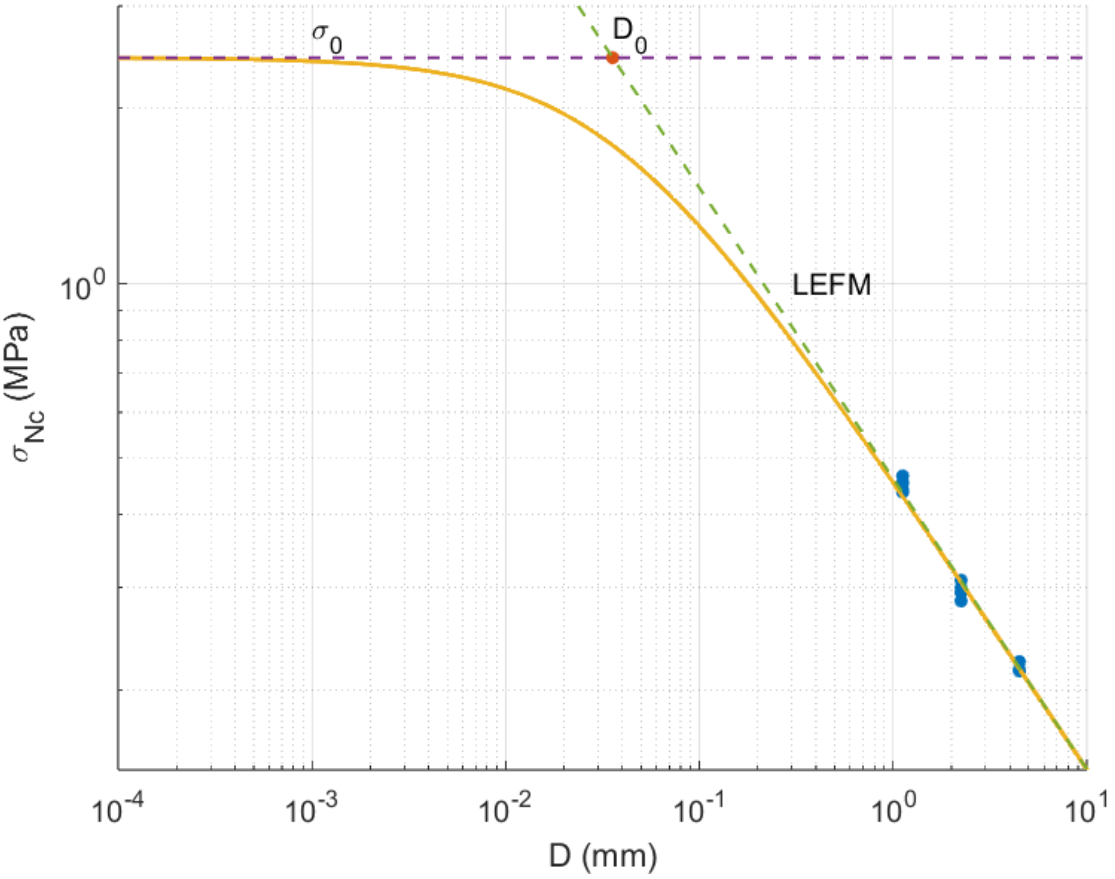

Figure 6.7: The Bažant size effect law curve of interlaminar Mode I fracture of IM7/977-3 0UD laminates

Therefore, for IM7/977-3 laminates with a thickness larger than 1mm, it is appropriate to directly use LEFM to predict the fracture load.

Size	D (mm)	β	LEFM Prediction (MPa)	SEL Prediction (MPa)	Error %
S	1.12	31.4	0.436	0.429	+1.58
M	2.24	62.8	0.308	0.306	+0.79
L	4.48	125.6	0.218	0.217	+0.40

Table 6.8: Brittleness of DCB coupons and the comparison between LFEM and SEL predictions

Chapter 7

MODE II INTERLAMINAR FRACTURE

This chapter aims to discuss the test results, finite element method simulation, and size-effect analysis of the ENF test of IM7/977-3 0-degree unidirectional laminates, which is dominated by the Mode II interlaminar fracture. This study defines the dimension variable D as the thickness of the ENF coupon $2h$.

7.1 Experimental Setup

The ENF test is conducted by Instron 5585H load frame with a 2kN load cell following ASTM D7905 standard. The fixture used in this test is a standard 3-point bending fixture, as shown in Fig. 7.1. The load cell is balanced prior to loading, and once the coupon is placed on the lower fixture, the upper fixture is slightly descended until the load frame shows little positive value. A ∼10N pre-compression is applied to ensure good contact between the coupon and fixture.

The ENF test is load controlled. The coupons are designed to break between two to ten minutes. This designated time interval saves time but still meets the quasi-static loading condition. The load control setting of the ENF test is displayed in Tab. 7.1.

Size	D (mm)	$\dot{P}$ (N/min)
S	1.12	125
M	2.24	250
L	4.48	500

Table 7.1: The load control setting of ENF test

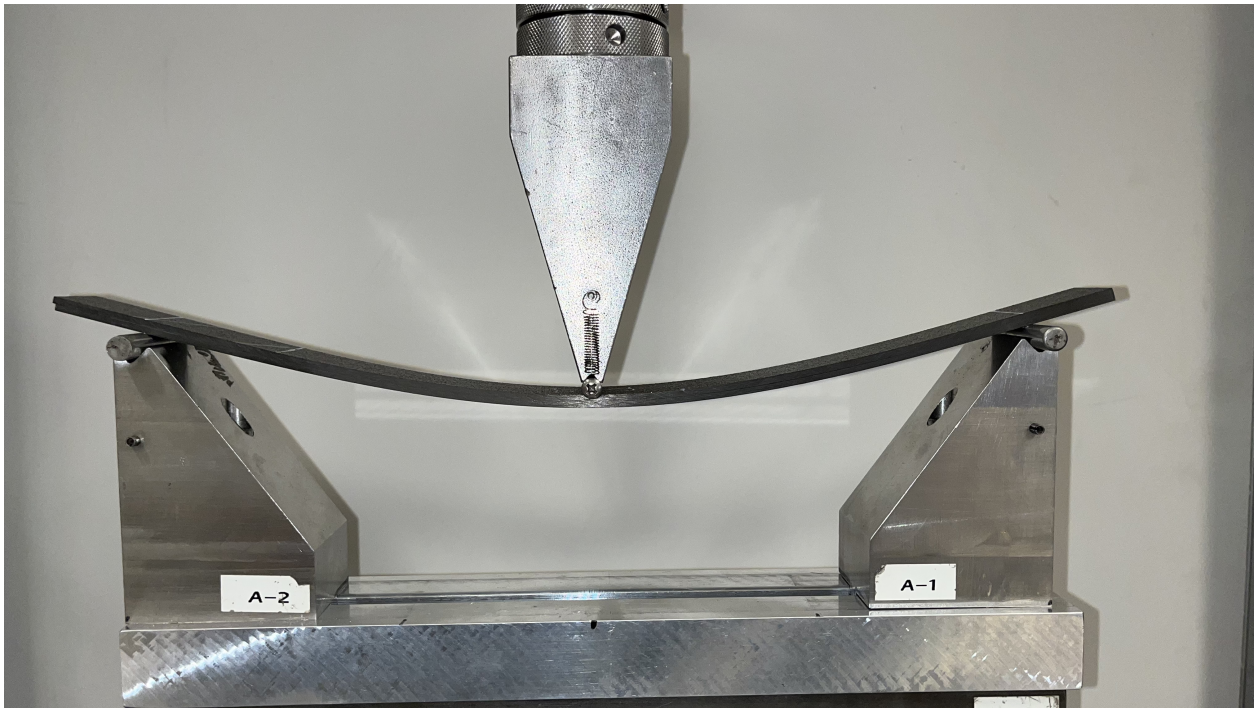

Figure 7.1: The 3-point bending setup for ENF tests

Besides standard load measurement, the strain field is also analyzed by DIC. A Nikon D5600 DSLR camera with a Nikon AF micro 200 mm lens is set in front of the specimen and 2-second interval photo shooting is used to record the change of the DIC grid pattern on the ENF coupon.

7.2 Test Results

The results of ENF tests are displayed in Table. 7.2 and Fig. 7.2. Compared to DCB tests, the results of ENF tests show a larger scattering. A possible explanation is that since the plies are laid up manually, the strength of the interlaminar bonding is not even through the interface, and compared to tensile loading in the DCB tests, shear loading in the ENF tests is more sensitive to the variation in interlaminar bonding strength. Besides that, the error of the position where 3-point bending fixtures contact the coupons can also contribute to the

variation of test results.

Size	D (mm)	Number of Coupons Tested	Mean Fracture Load (N)	Coefficient of Variation %
S	1.12	4	390.6	1.35
M	2.24	4	625.1	3.10
L	4.48	5	1039.8	6.80

Table 7.2: Fracture load of ENF coupons

Compared to the DCB tests, in which the cracks propagate stably and smoothly, the crack propagation in the ENF tests is unstable. Starting from $\alpha_0 = 0.15$, the crack propagates to $\alpha \approx 0.7$ in a sudden and dissipates great acoustic energy. Fig. 7.3 displays the zoomed end of a failed ENF coupon, from which the separation of the upper and lower halves of the ENF coupon can be clearly observed.

The DIC analysis yields the change in the strain field around the crack tip with increasing loading, and Fig. 7.4 displays the xy-direction shear strain field at the instant just before initial crack propagation, from which significant strain localization is observed in front of the crack tip.

7.3 Finite Element Method Simulation

The Abaqus-assisted J-integral method is also used to determine g and g' for DENT coupons. In this test, D is defined as the thickness of the coupon $2h$, and the nominal stress is defined as

$$\sigma_{Nc} = \frac{P}{2bh} \tag{7.1}$$

Similar to the case of the DCB tests, the effective stiffness E' is defined as $E' = E_{1T} =$ 164 GPa.

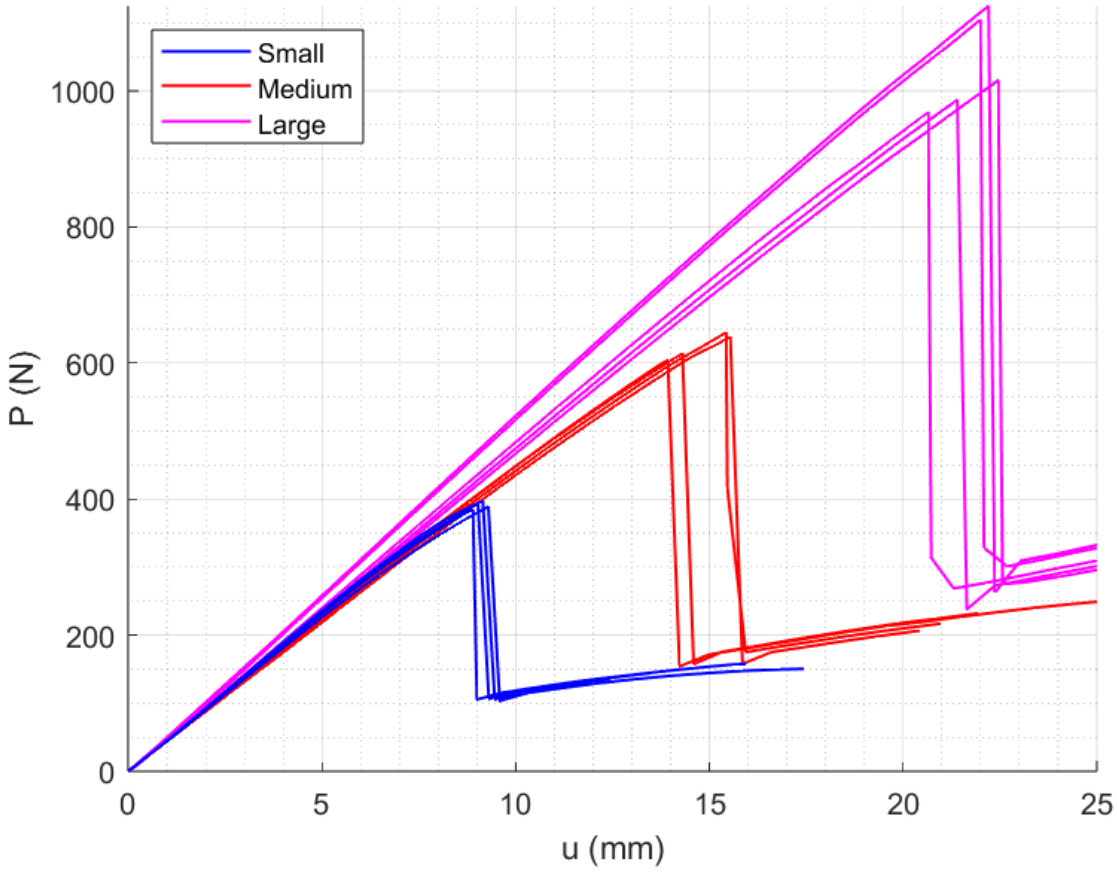

Figure 7.2: The load-displacement curves of ENF coupons of three sizes

The side projection of the ENF coupon between the left and right 3-point bending supports is modeled in Abaqus. The designated crack tip and crack seam are defined at the middle of the left edge. To simulate the ENF test, the bottom left and bottom right corners are set to be simply supported, and vertical displacement control of -1 mm is set at the middle of the top edge. The contacting interaction is set on the seam with a friction penalty of $\mu = 0.3$. The boundary condition setting is displayed in Fig. 6.4.

The laminate is modeled as a linear elastic transversely isotropic homogeneous material with the properties shown in Table. 7.3. A meshing strategy that is similar to the one used

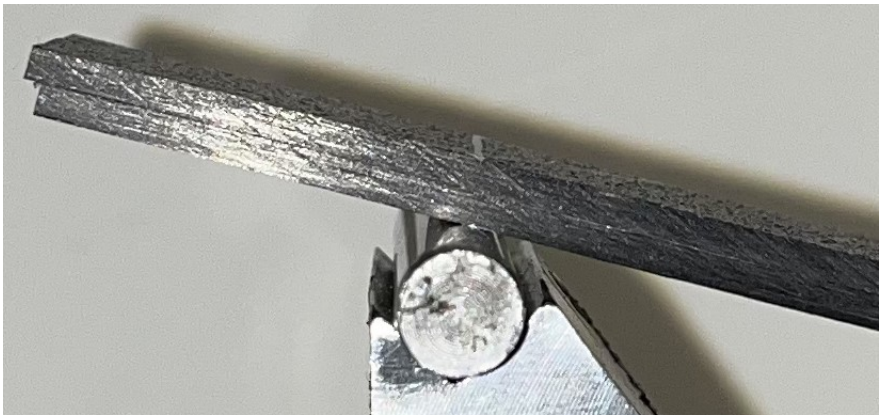

Figure 7.3: A large-sized ENF coupon after the test

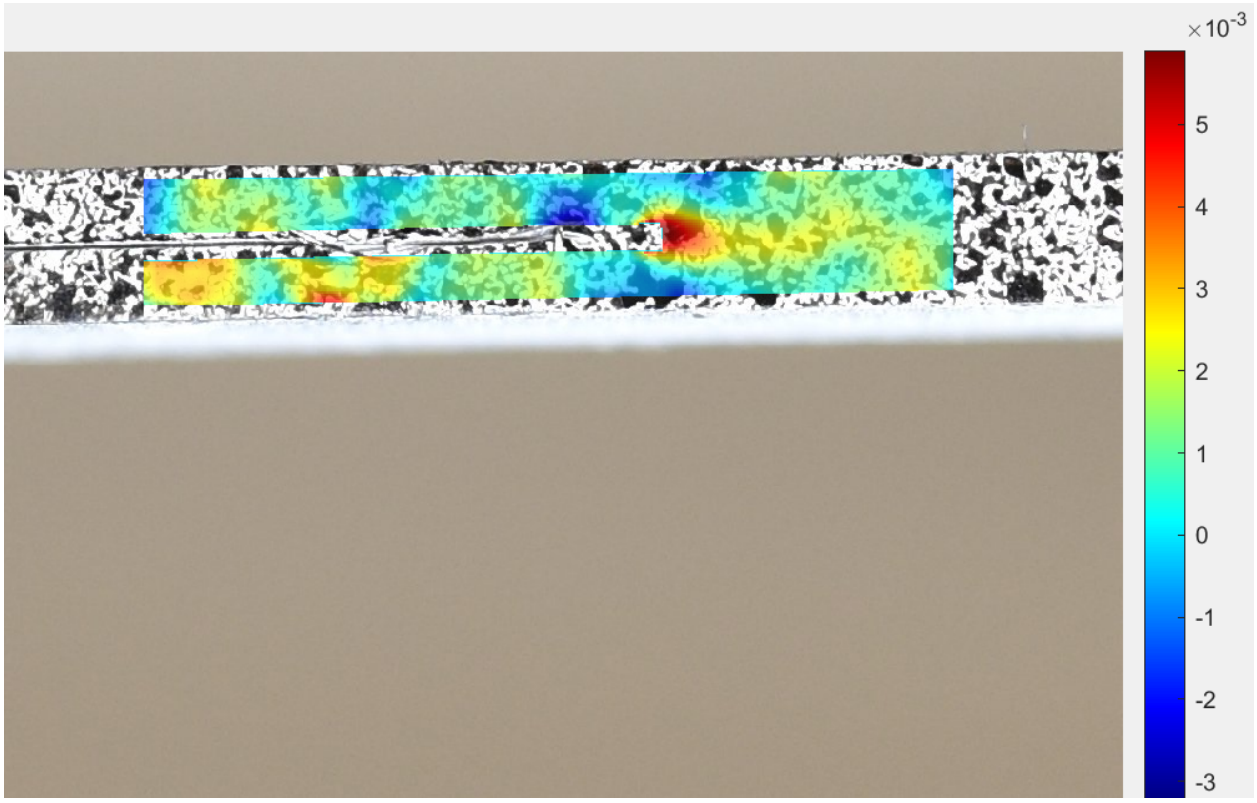

Figure 7.4: The ϵ_{xy} strain field around the crack tip of a large-sized ENF coupon

Figure 7.5: The boundary condition setting of Abaqus simulation of ENF coupons

for DCB test simulation is used, which is displayed in Fig. 6.5.

E_1 (GPa)	E_2&E_3 (GPa)	G_{12}&G_{13} (GPa)	G_{23} (GPa)	ν_{12}&ν_{13}	ν_{23}
164	8.98	5.01	3.326	0.320	0.350

Table 7.3: Material properties used in Abaqus simulation of ENF coupons

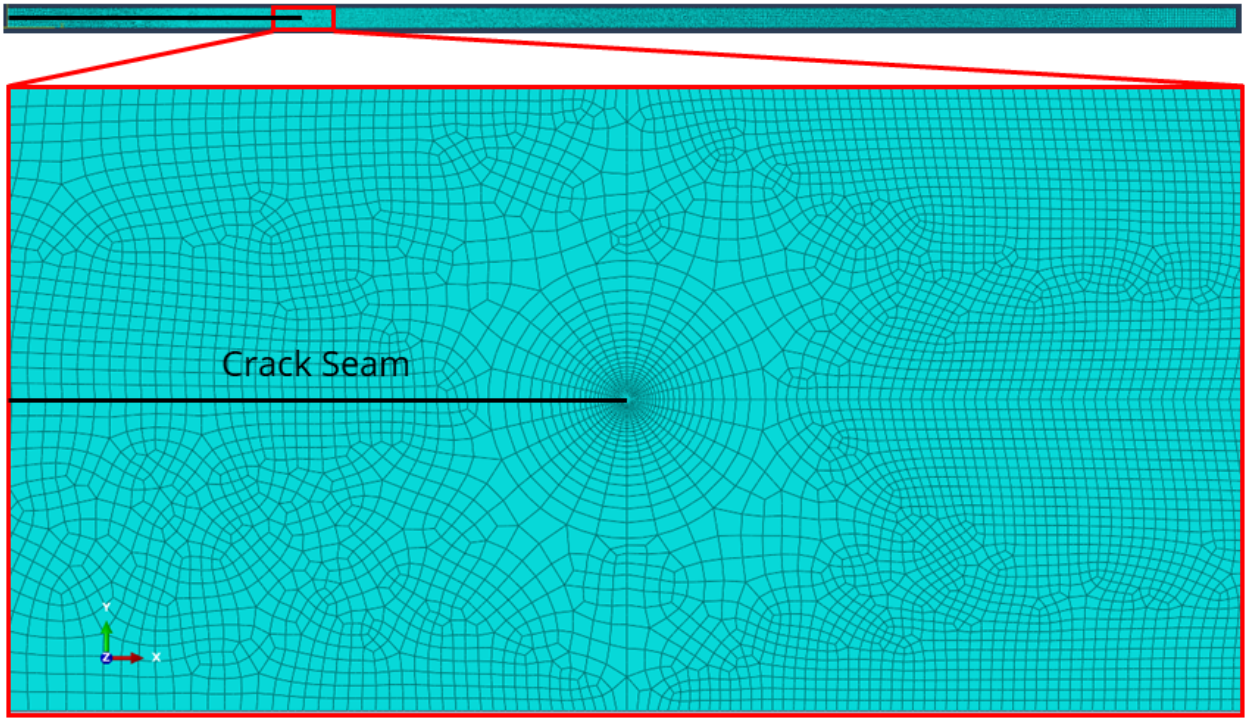

Figure 7.6: The meshing condition setting of Abaqus simulation of ENF coupons

Table. 7.4 and 7.5 conclude all the computed J-integral, the reaction force, and $g(\alpha_0)$

and $g'(\alpha_0)$ determined from Eq. 2.11 and 2.12. Due to the friction penalty on the contacting surfaces of the crack, there is a minor variation in the $g(\alpha_0)$ and $g'(\alpha_0)$ values. The average values of $g(\alpha_0)$ and $g'(\alpha_0)$ of the three-sizes are used for the Bažant size effect law.

Size	D (mm)	$J(\alpha_0)$ (N/mm)	$P(\alpha_0)$ (kN)	$g(\alpha_0)$
S	1.12	13.22×10^{-3}	58.9	438
M	2.24	6.62×10^{-3}	58.8	439
L	4.48	3.31×10^{-3}	58.8	439

Table 7.4: The J-integrals, reaction forces, and dimensionless energy release rate of ENF coupons with $\alpha_0 = 0.2$

Size	D (mm)	$J(\alpha_0 - \Delta\alpha)$ (N/mm)	$J(\alpha_0 + \Delta\alpha)$ (N/mm)	$P(\alpha_0 - \Delta\alpha)$ (kN)	$P(\alpha_0 + \Delta\alpha)$ (kN)	$g'(\alpha_0)$
S	1.12	13.11×10^{-3}	13.3×10^{-3}	58.9	58.8	5.69×10^{3}
M	2.24	6.57×10^{-3}	6.68×10^{-3}	58.9	58.8	5.70×10^{3}
L	4.48	3.29×10^{-3}	3.34×10^{-3}	58.9	58.8	5.70×10^{3}

Table 7.5: The J-integrals and reaction forces of ENF coupons with $\alpha_0 \pm \Delta\alpha$ and the computed dimensionless energy release rate gradient

7.4 Analysis

The weighted linear regression is used for ENF test results as well. The linear regression result of the ENF test is displayed in Fig. 7.7 and Tab. 7.6. Compared to the linear regression of DCB test results, the ENF results are more scattered, especially for the large-sized coupons, probably because of the previously discussed variation in the bonding strength of the interlaminar interface.

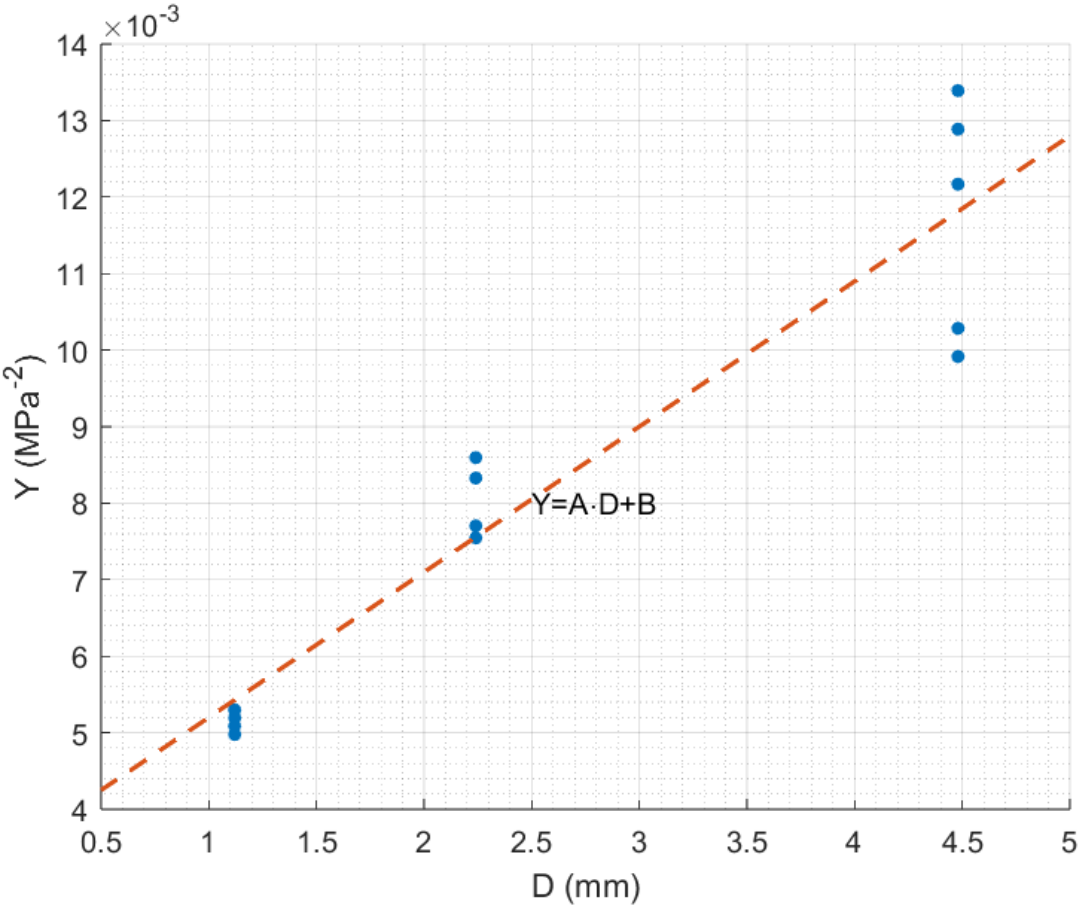

Figure 7.7: The linear regression of ENF test results based on Eq. 2.13

A (MPa^{-2}mm^{-1})	B (MPa^{-2})	R^2
0.0019	0.0033	0.897

Table 7.6: The linear regression of ENF test results based on Eq. 2.13

Tab. 7.7 shows the key size effect parameters determined by Eq. 2.14, 2.15, 2.16 and 2.17. Based on the determined properties, the SEL curve fit is plotted to show demonstrate the influence of FPZ, as shown in Fig. 7.8, and the brittleness of DENT coupons is computed and displayed in Table. 7.8.

G_{IIc} (N/mm)	C_f (mm)	σ_0 (MPa)	D_0 (mm)
1.41	0.134	17.4	1.74

Table 7.7: Key size effect parameters of interlaminar Mode II fracture of IM7/977-3 0UD laminates

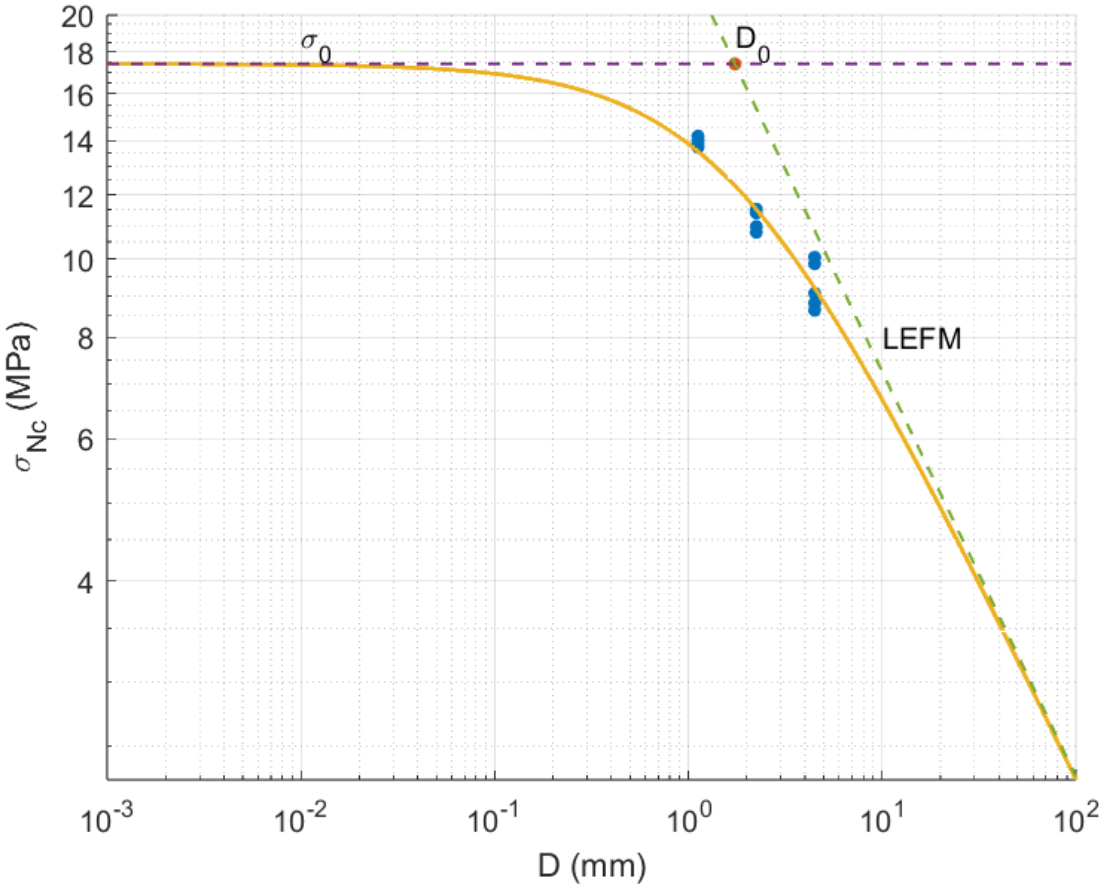

Figure 7.8: The Bažant size effect law curve of interlaminar Mode II fracture of IM7/977-3 0UD laminates

Based on the size effect law curve and the brittleness table, it can be concluded that similar to the DENT coupons, the fracture behavior of the ENF coupons is between the behavior of perfectly ductile and the behavior of perfectly brittle materials, and LEFM tends

Size	D (mm)	β	LEFM Prediction (MPa)	SEL Prediction (MPa)	Error %
S	1.12	0.645	21.7	13.6	+59.7
M	2.24	1.290	15.3	11.5	+33.2
L	4.48	2.580	10.8	9.2	+17.8

Table 7.8: Brittleness of ENF coupons and the comparison between LFEM and SEL predictions

to overestimate the fracture loads of all three-sizes. Therefore, for IM7/977-3 laminates with a thickness of less than 100 mm, which is the most common case, the LEFM cannot be recklessly used. Compared to the Mode I interlaminar fracture, the Mode II interlaminar fracture is affected more by the existence of FPZ.

Chapter 8

FUTURE WORK AND CONCLUSION

8.1 Future Work

8.1.1 Mode I Intralaminar Fracture of ±45-Degree Plies

This study covers the Mode I intralaminar fracture test of $[90]_{12}$ and $[0/90_5]_s$ (dominated by 0-degree plies) laminates, but the IM7/977-3 fracture behavior of the other most common component existing in the quasi-isotropic laminate, ±45 plies, have not been studied yet. By testing the Mode I intralaminar fracture of ±45-degree plies using SENT or DENT tests, it is possible to predict the fracture energy and size effect of IM7/977-3 of any quasi-isotropic laminate composed of 0-, 90- and ±45-degree plies under tensile loading.

8.1.2 Mode III Intralaminar and Interlaminar Fracture

There are very few studies focusing on Mode III fracture, however, the tearing/torsional load is a relatively common type of load in the aircraft, so the investigation of the Mode III fracture of IM7/977-3 is also important and can further extend the understanding of the fracture behavior of IM7/977-3 laminates. The Mode III intralaminar fracture can be investigated by applying the torsional load on the single-edge or double-edge notched coupons using the Shore Western 306 Series load frame, but the investigation of the Mode III interlaminar fracture is more challenging. Fig. 8.1 shows the schematic of Edge Crack Torsion (ECT) designed by Lee [23], but Audd et al. pointed out that correction is required for ECT tests, which increases the complexity of this test. [6]

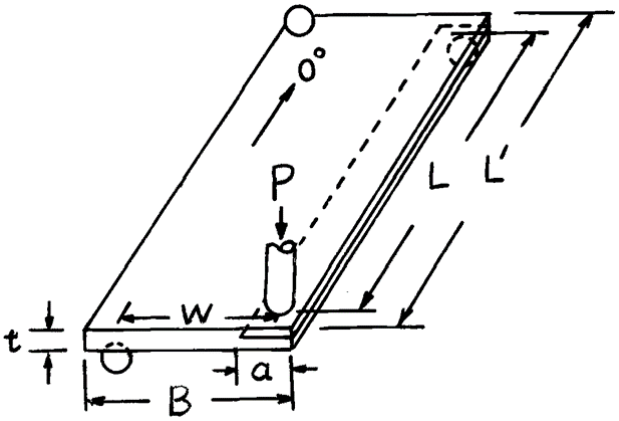

Figure 8.1: Schematic of the edge crack torsion test [23]

8.1.3 Statistical Size Effect Test

This study only covers the energetic (Type II) size effect, which applies to the structures with an initial crack. However, for the structures made of quasibrittle material without any initial crack, there exists another energetic-statistical size effect (Type I), which involves the influence of Weibull's distribution of material strength. [37] The tests to investigate the Type I size effect are similar to the one for Type II but without the pre-created crack on test coupons.

8.2 Conculusion

Quasi-static size effect tests including SENT, DENT, DCB, and ENF are conducted to investigate the fracture behavior of IM7/977-3 in different modes, including the Mode I matrix-dominated intralaminar fracture, Mode I fiber-dominated intralaminar fracture, Mode I interlaminar fracture, and Mode II interlaminar fracture with an initial crack. Fig. 8.2 displays the complete normalized size effect curve of four modes.

From Fig. 8.2 and the brittleness tables Tab. 4.8, 5.8, 6.8, and 7.8, several findings can be summarized:

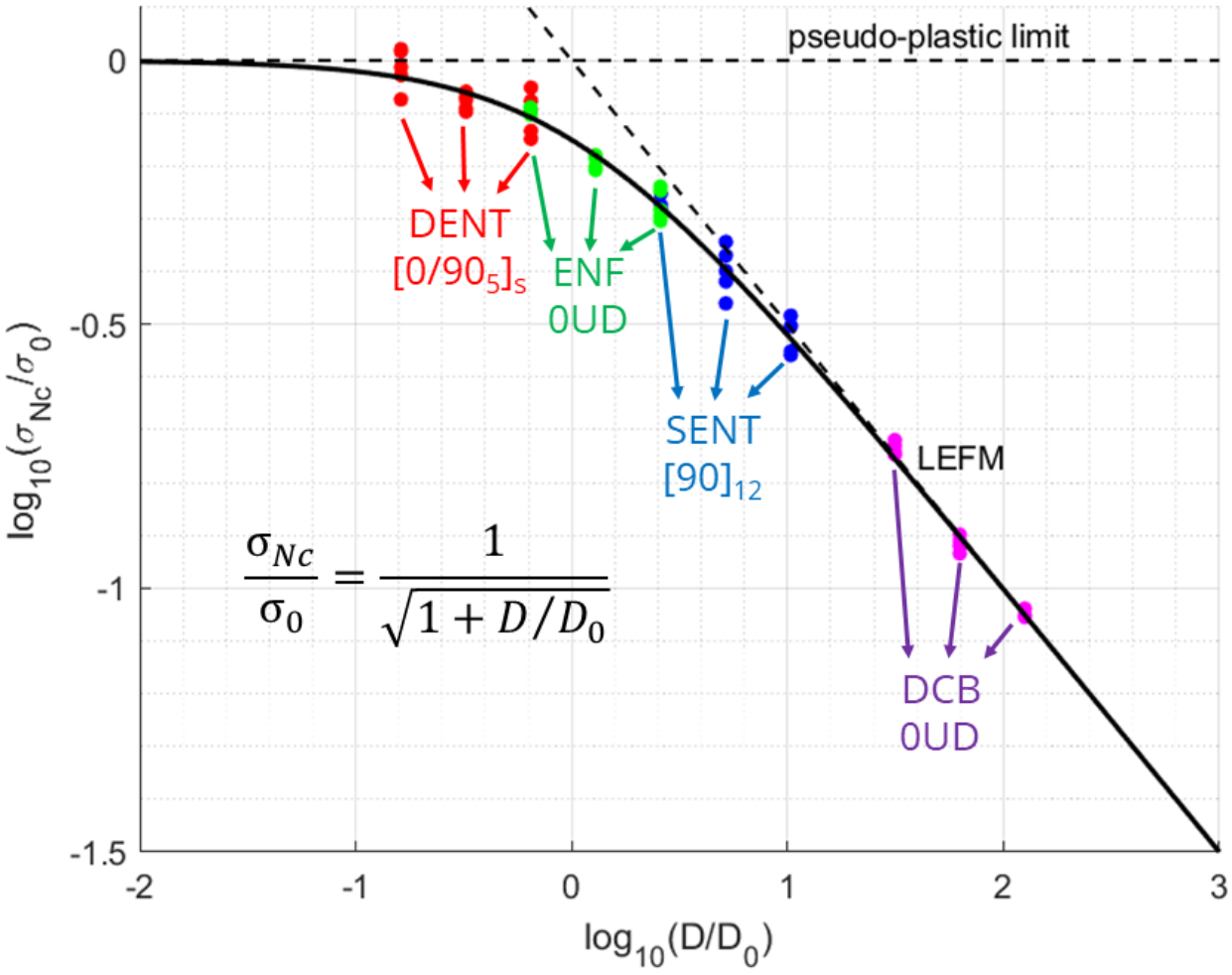

Figure 8.2: Normalized Bažant size effect law fit of SENT, DENT, DCB, and ENF test results

- Due to the anisotropy of IM7/977-3, the fracture properties of the laminate are different for each direction and each mode.

- The fiber-dominated Mode I intralaminar fracture ($C_f \approx 14.99$ mm) and Mode II interlaminar fracture ($C_f \approx 0.1339$ mm) are in the transition zone of the size effect curve because their sizes are comparable to the corresponding effective FPZ sizes. Their fracture behaviors are neither brittle nor ductile. The prediction of the fracture load of these modes must be conducted extremely carefully.

- The matrix-dominated Mode I intralaminar fracture ($C_f \approx 0.7698$ mm) is slightly deviated from the LEFM prediction and approaching the transition zone. LEFM can still make a crude estimation of the fracture load, but a conservative factor of safety must be designated to ensure the 90-degree plies can withstand the load.

- The Mode I interlaminar fracture ($C_f \approx 7.337$ μm) is close to the fracture behavior of perfectly brittle material, and LEFM can provide an accurate estimation of the fracture load.

Other notable findings of this study include:

- The fracture energies of the four modes are:

    1. Matrix-dominated Mode I intralaminar fracture of $[90]_{12}$ laminate: $G_{Ic} = 0.3840$ N/mm
    2. Fiber-dominated Mode I intralaminar fracture of $[0/90_5]_s$ laminate: $G_{Ic} = 312.8$ N/mm
    3. Mode I interlaminar fracture of 0-degree unidirectional laminate: $G_{Ic} = 0.1674$ N/mm
    4. Mode II interlaminar fracture of 0-degree unidirectional laminate: $G_{IIc} = 1.409$ N/mm

- The fiber-dominated Mode I intralaminar fracture involves extra modes of energy dissipation such as fiber being stretched out from the laminate, so significant scattering of test results is observed, and the size effect law only provides a crude estimation of G_{Ic} and C_f.

- Compared to the Mode I interlaminar fracture, the Mode II interlaminar fracture is more sensitive to the variation of strength between the interlaminar interfaces.

- The crack propagation of the matrix-dominated and the fiber-dominated Mode I intralaminar fractures, as well as the Mode II interlaminar fracture, are unstable, but the crack propagation of the Mode I interlaminar fracture is stable.

BIBLIOGRAPHY

[1] Daniel Adams. Composites testing as part of a building block approach, part 1: Coupon-level testing, 2021. Last accessed 3 June 2023.

[2] Almar Almarnaess. Fatigue handbook: offshore steel structures. 1985.

[3] Michael F Ashby and D Cebon. Materials selection in mechanical design. *MRS Bull*, 30(12):995, 2005.

[4] ASTM. Standard test method for determination of the mode ii interlaminar fracture toughness of unidirectional fiber-reinforced polymer matrix composites1. Designation: D7905/D7905M-19.

[5] ASTM. Standard test method for mode i interlaminar fracture toughness of unidirectional fiber-reinforced polymer matrix composites. Designation: D5528/D5528M-21.

[6] Clay Audd, Barry D Davidson, James G Ratcliffe, and Michael W Czabaj. Reexamination of the edge crack torsion test for determining the mode iii delamination toughness of laminated composites. *Engineering Fracture Mechanics*, 215:138–150, 2019.

[7] Jens Bachmann, Carme Hidalgo, and Stéphanie Bricout. Environmental analysis of innovative sustainable composites with potential use in aviation sector—a life cycle assessment review. *Science China Technological Sciences*, 60:1301–1317, 2017.

[8] Zdenek P Bažant, Jia-Liang Le, and Marco Salviato. *Quasibrittle fracture mechanics and size effect: a first course*. Oxford University Press, 2021.

[9] Jeremy Brockmann and Marco Salviato. The gap test–effects of crack parallel compression on fracture in carbon fiber composites. *Composites Part A: Applied Science and Manufacturing*, 164:107252, 2023.

[10] S Burtscher, B Chiaia, JP Dempsey, G Ferro, VS Gopalaratnam, P Prat, K Rokugo, VE Saouma, V Slowik, L Vitek, et al. Rilem tc qfs 'quasibrittle fracture scaling and size effect'-final report. *Materials and structures*, 37:547–568, 2004.

[11] Stephen B Clay and Philip M Knoth. Experimental results of quasi-static testing for calibration and validation of composite progressive damage analysis methods. *Journal of Composite Materials*, 51(10):1333–1353, 2017.

[12] CYCOM®. CYCOM® 977-3 epoxy resin system.

[13] Rachael Geerts. Vacuum bagging basics, 2019. Last accessed 3 June 2023.

[14] Kevin Guo, Yao Qiao, and Marco Salviato. Scaling of fatigue crack growth in pristine epoxy. In *Proceedings to 33rd Annual Technical Conference, 18th US-Japan Conference on Composite Materials ASTM D*, volume 30, 2018.

[15] Ryan Howe. Experimental investigation of mode ii fracture and fatigue in unidirectional carbon/epoxy composite beams. 2021.

[16] George R Irwin. Analysis of stresses and strains near the end of a crack traversing a plate. 1957.

[17] Seunghyun Ko, Kenrick Chan, Reed Hawkins, Rohith Jayaram, Christopher Lynch, Reda El Mamoune, Minh Nguyen, Nicolay Pekhotin, Natania Stokes, D Wu, et al. Experimental and numerical characterization of the intra-laminar fracturing behavior in discontinuous fiber composite structures. In *Proceedings of the 33th ASC Conference, Seattle, WA, USA*, pages 24–26, 2018.

[18] Seunghyun Ko, James Davey, Sam Douglass, Jinkyu Yang, Mark E Tuttle, and Marco Salviato. Effect of the thickness on the fracturing behavior of discontinuous fiber composite structures. *Composites Part A: Applied Science and Manufacturing*, 125:105520, 2019.

[19] Seunghyun Ko, Troy Nakagawa, Zhisong Chen, William B Avery, Ebonni J Adams, Matthew R Soja, Michael H Larson, Chul Y Park, Jinkyu Yang, and Marco Salviato. Effects of average number of platelets through the thickness and platelet width on the mechanical properties of discontinuous fiber composites. *arXiv preprint arXiv:2302.02574*, 2023.

[20] Seunghyun Ko, Jinkyu Yang, Mark E Tuttle, and Marco Salviato. Effect of the platelet size on the fracturing behavior and size effect of discontinuous fiber composite structures. *Composite Structures*, 227:111245, 2019.

[21] Laszlo P Kollar and George S Springer. *Mechanics of composite structures*. Cambridge university press, 2003.

[22] Yuta Kumagai, Sota Onodera, Marco Salviato, and Tomonaga Okabe. Multiscale analysis and experimental validation of crack initiation in quasi-isotropic laminates. *International Journal of Solids and Structures*, 193:172–191, 2020.

[23] Shaw M Lee. An edge crack torsion method for mode iii delamination fracture testing. *Journal of Composite Technology & Research*, 15(3):193–201, 1993.

[24] Weixin Li, Yao Qiao, Joel Fenner, Kyle Warren, Marco Salviato, Zdeněk P Bažant, and Gianluca Cusatis. Elastic and fracture behavior of three-dimensional ply-to-ply angle interlock woven composites: Through-thickness, size effect, and multiaxial tests. *Composites Part C: Open Access*, 4:100098, 2021.

[25] Cory Hage Mefford, Yao Qiao, and Marco Salviato. Failure behavior and scaling of graphene nanocomposites. *Composite Structures*, 176:961–972, 2017.

[26] Troy Nakagawa, Seunghyun Ko, Cory Slaughter, Talal Abdullah, Guy Houser, and Marco Salviato. Effects of aging on the mechanical and fracture properties of chopped fiber composites made from repurposed aerospace prepreg scrap and waste. *Sustainable Materials and Technologies*, 33:e00470, 2022.

[27] Troy Nakagawa, Erik Poulin, Talbot Rueppel, Zhisong Chen, Juliet Swinea, Mark O'Brien, Guy Houser, Geoffrey Wood, Malloree Weinheimer, Pouria Bahmani, et al. Effects of thermal modification on the flexure properties, fracture energy, and hardness of western hemlock. *arXiv preprint arXiv:2304.00052*, 2023.

[28] Yao Qiao, Kaiwen Guo, and Marco Salviato. Size effect and scaling in quasi-static and fatigue fracture of graphene polymer nanocomposites. *Polymer Composites*, 2023.

[29] Yao Qiao and Marco Salviato. Strength and cohesive behavior of thermoset polymers at the microscale: A size-effect study. *Engineering Fracture Mechanics*, 213:100–117, 2019.

[30] Yao Qiao and Marco Salviato. Study of the fracturing behavior of thermoset polymer nanocomposites via cohesive zone modeling. *Composite Structures*, 220:127–147, 2019.

[31] Yao Qiao, Qiwei Zhang, TROY Nakagawa, and MARCO Salviato. A size effect study on the splitting crack initiation and propagation in off-axis layers of composite laminates. In *36th American Society for Composites Conference*, 2021.

[32] Yao Qiao, Qiwei Zhang, and Marco Salviato. Effects of in-situ stress state on the plastic deformation, fracture, and size scaling of thermoset polymers and related fiber-reinforced composites. In *ASC 35th Technical Conference*, 2020.

[33] James R Rice. A path independent integral and the approximate analysis of strain concentration by notches and cracks. 1968.

[34] Marco Salviato, Viet T Chau, Weixin Li, Zdeněk P Bažant, and Gianluca Cusatis. Direct testing of gradual postpeak softening of fracture specimens of fiber composites stabilized by enhanced grip stiffness and mass. *Journal of Applied Mechanics*, 83(11), 2016.

[35] Marco Salviato, Kedar Kirane, Shiva Esna Ashari, Zdeněk P Bažant, and Gianluca Cusatis. Experimental and numerical investigation of intra-laminar energy dissipation and size effect in two-dimensional textile composites. *Composites Science and Technology*, 135:67–75, 2016.

[36] Marco Salviato, Kedar Kirane, Zdeněk P Bažant, and Gianluca Cusatis. Mode i and ii interlaminar fracture in laminated composites: a size effect study. *Journal of Applied Mechanics*, 86(9), 2019.

[37] Waloddi Weibull. The phenomenon of rupture in solids. *IVA Handlingar*, 153, 1939.

[38] Harold M Westergaard. Bearing pressures and cracks: Bearing pressures through a slightly waved surface or through a nearly flat part of a cylinder, and related problems of cracks. 1939.